Structure and Electrical Conductivity of Mn-based Spinels Used as Solid Oxide Fuel Cell Interconnect Coatings

By
Yadi Wang, B. ENG

A Thesis Submitted to the school of Graduate Studies in Partial Fulfillment of the Requirements for the Degree Master of Applied Science

McMaster University

MASTER OF APPLIED SCIENCE (2013) McMaster University
(Materials Science and Engineering) Hamilton, Ontario

TITLE: Structure and Electrical Conductivity of Mn-based Spinel Used as Solid Oxide Fuel Cell Interconnect Coatings

AUTHOR: Yadi Wang, B.Eng (University of Science & Technology, Beijing)

SUPERVISOR: Professor Anthony Petric

NUMBER OF PAGES: XIV, 104

Abstract

At solid oxide fuel cell (SOFC) operating temperatures (650°C--800°C), the chromia scale growth on the interconnect surface and chromium poisoning of cathode can lead to performance degradation of the whole cell. A spinel coating can be effective for blocking chromium outward diffusion to overcome this issue. In this thesis, two spinel-forming systems, Zn-Mn-O and Co-Cu-Mn-O were studied to identify a suitable coating.

In-situ high temperature XRD was used to identify the phases in the Zn-Mn-O system between 600°C and 1300°C. The results showed that cubic spinel phase was stable only at high temperatures (above 1200°C) and when the temperature decreases, the cubic phase tends to deform to tetragonal structure. In addition, the conductivity results showed low conductivities (below 3 S/cm) at SOFC operating temperature. Thus, the Zn-Mn-O system is not suitable for SOFC interconnect coatings.

Another potential coating material analyzed was the Co-Cu-Mn-O system. This system exhibited promising conductivity values (above 50 S/cm). Electrodeposition was used to apply Co-Cu-Mn-O coatings on both ferritic stainless steel (16% -- 18% chromium) and chromium-based alloy (95% chromium and 5% iron) followed by oxidation in air at 800°C. The spinel coating formed nicely on the stainless steel substrate. However, on the chromium plate, nitride formation, blistering and metal isolation were the common problems that occurred during the oxidation process. In order to improve the quality of coating on the chromium alloy, different heat treatments were explored, such as annealing in reducing atmosphere, oxidation in pure oxygen / mixed gas and decreasing the oxidation temperature. The objective of modifying the heat treatment was to produce adherent, dense coatings.

Acknowledgements

I would like to first express my gratitude to my supervisor, Dr Anthony Petric for offering me the opportunity with this project. Thanks for his mentorship, support as well as extraordinary advice during the two years' study. I really appreciate his vast knowledge in many areas and assistance in writing this thesis.

I would also like to thank Dr Yurij Mozharivskyj from the Chemistry department for his great contribution of high temperature XRD equipment and analysis. His patience and experience provided a valuable asset.

In addition, I would like to thank the members of the Canadian Center for Electron Microscopy for their guidance with SEM imaging, especially Chris Butcher and Dr de Silveira for their valuable advice. I would also like to thank the members in McMaster Analytical X-Ray Diffraction Facility (MAX) for their work of characterization of the samples.

Special thanks to the staff in the Materials Science and Engineering department, their endless dedication provided me with unforgettable experience.

I would also like to thank the members in my research group, Dr Ping Wei, Dr Simon Joshi, Dr Amin Mali, Xavier Michaud and Meng Ren. Their support and great advice helped me to conduct the research smoothly.

Lastly, but most importantly, I would like to thank my beloved parents. Their

endless sacrifice and support gave me the courage and confidence to overcome all the problems during my study and life.

Table of Contents

List of Tables

List of Figures

Chapter 1

Introduction

The principle of the fuel cell was first proposed by German-Swiss scientist Christian Friedrich Schönbein in 1838 and a year later, the first crude fuel cell was demonstrated by Welsh physicist William Grove. The fuel cell converts chemical energy, usually hydrogen as fuel gas, directly into electrical energy without combustion, and thus the fuel cells are not only high in efficiency but also environmentally friendly. In contrast to the battery which has to be recharged or discarded when used up, the fuel cell can continuously produce electricity as long as there is a fuel supply.

One of the first real applications for the fuel cell was by NASA for generating power in spacecraft and satellites. Since then it has been used in many other applications. Nowadays, the usage of fuel cells can be categorized into three broad areas: portable power generation (including military applications and auxiliary power units), stationary power generation and power for transportation (propulsion power to a vehicle).

The solid oxide fuel cell (SOFC) was demonstrated in 1937 by Bauer and Preis (Irvine & Connor, 2013) and for decades, it was regarded to hold the greatest potential of any fuel cell technology. SOFCs are characterized by the use of a solid oxide electrolyte to conduct oxygen anions from the cathode to the anode which necessitates high temperatures (operation around 800^oC). Unlike most other fuel cells, SOFCs can have multiple geometries. Besides the traditional sandwiched planar fuel cell design, they also can be made in tubular geometries that are easier to seal. In addition, the SOFC has the ability to use hydrocarbon-based gas as fuel instead of pure hydrogen, which makes it more competitive than other traditional power-generating devices.

The SOFC has a wide variety of potential power generation applications. It can be used as back up energy for hospitals, office buildings or residences. With the usage of SOFCs, the cost on long distance electrical transportation can be reduced; furthermore, the heat generated from the high temperature reaction can be recycled for steam reforming or water heating. Companies such as eBay and Google have been using SOFC technology to provide approximately 15% of their electricity since 2010, and further evaluation is still ongoing.

However, some issues limit the commercial headway of SOFCs, one of which is called cathode poisoning. From the 1990s, investigators made it possible to replace the ceramic interconnect with a low cost, easier to fabricate metallic interconnect between single cells in a stack. This interconnect is a chromium-based alloy. However the serious problem is that chromium oxide formed on the interconnect surface can react with dry or humid air to produce volatile species that poison the cathode and degrade the performance of the whole cell. Thus a protective coating is needed on the interconnect surface. Investigators have found that the perovskite and spinel oxides are suitable coating materials (Shaigan et al, 2009). Although the perovskite has better properties, it is limited by the cost of materials and equipment. Spinel oxide is easier to apply, and the goal of this thesis is to produce a conductive, dense spinel coating on the interconnect.

Chapter 2

Review

2.1 Solid Oxide Fuel Cell (SOFC)

The solid oxide fuel cell (SOFC) is entirely solid-state and highly efficient. It has many advantages as a power-generation device: first, it produces no noise during operation since it has no moving parts; therefore noise pollution associated with power generation is also eliminated. Second, the SOFC has no strict requirements on fuel gas composition. Unlike some other types of fuel cells that need pure hydrogen, the SOFC can use variety of fuels, most of which are hydrocarbon-based fuels such as methane and propane. The third advantage is since SOFC operates at high temperatures, usually between 500^{o}C to 1000^{o}C, expensive platinum catalyst is not required. Also, the heat generated during operation can be used as a source of heat energy such as heating buildings.

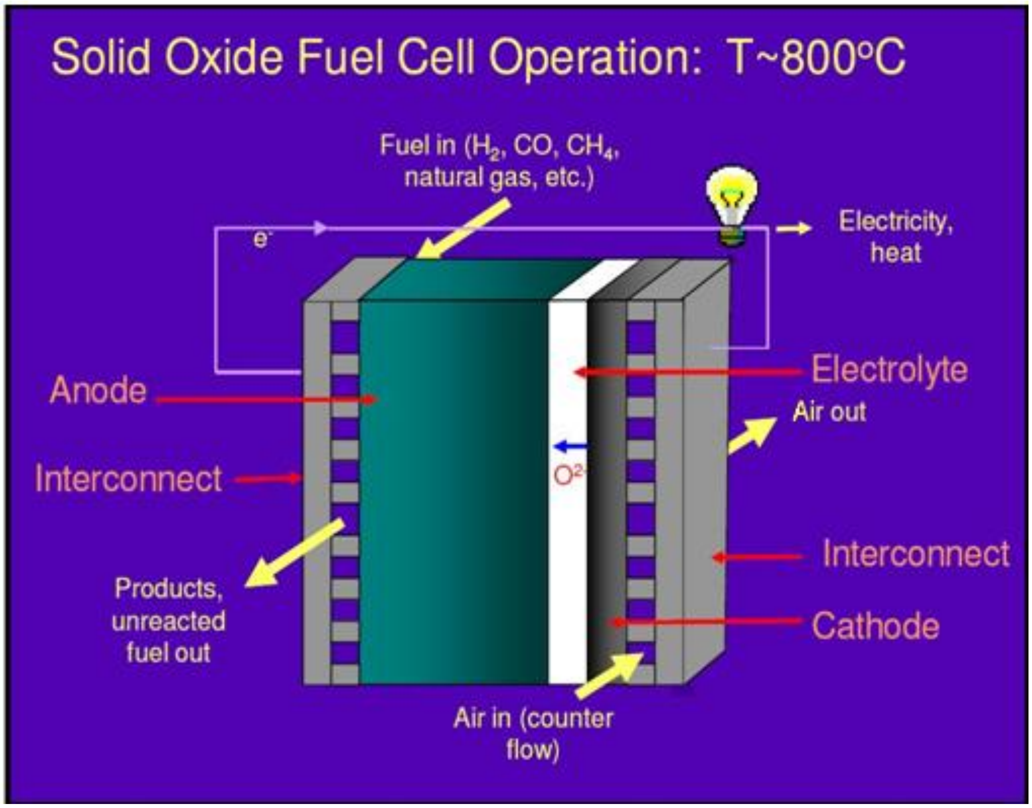

Figure 2.1 Solid oxide fuel cell (SOFC) working schematic diagram (Bateni, 2012)

Figure 2.1 shows the working schematic diagram of a SOFC. The oxygen (air) flows through the cathode side, undergoing a reduction reaction, as given in Equation 2-1. The oxygen ion transports through the porous cathode, then dense but ion-conductive electrolyte, and finally reaches the anode side where it reacts with the fuel gas to produce electricity, water and a small amount of carbon dioxide. Some of the exhausted gas gets recycled to reform the fuel. The process also generates the heat required by the fuel cell. As long as there is fuel, air and heat, the process continues producing clean, reliable affordable energy. The oxidation reactions are described in Equations 2-2 to 2-4.

$$1/2O_2 + 2e^- = O^{2-} \quad 2\text{-}1$$

$$H_2 + O^{2-} = H_2O + 2e^- \quad 2\text{-}2$$

$$CO + O^{2-} = CO_2 + 2e^- \quad 2\text{-}3$$

$$CH_4 + 4O^{2-} = CO_2 + 2H_2O + 8e^- \quad 2\text{-}4$$

2.2 Interconnect

In the fuel cell, the interconnect provides electrical connection between single cells inside the stack. Also it serves as a gas separator within the stack, with fuel gas flowing on one side and oxygen on the other side (Figure 2.2). There are several requirements for the interconnect: high electrical conductivity, chemical stability in both reducing and oxidizing environment, thermal expansion match to other cell components, high mechanical strength, and chemical stability with regard to other cell components (Singhal & Kendal, 2003).

Early interconnects were perovskite ceramics. In the 1990s, investigators found that by decreasing the thickness of the electrolyte to micron scale, the operation temperature of SOFC could be decreased from 1000°C to 800°C (Souza et al, 1997). This made it possible to use the metallic interconnects (Zhu & Deevi, 2003; Fergus, 2004). Compared with ceramic interconnects, the metallic interconnects benefit from lower cost, easier fabrication and higher electrical/thermal conductivity (Quadakkers et al, 2003). Since the operation temperature is still high, the metal selected must be resistant to high temperature oxidation and hot corrosion (Shaigan et al, 2009).

Aluminum, silicon and chromium can all form a protective oxide layer to prevent rapid oxidation. Aluminum-based metals are not suitable because alloys containing aluminum have extremely slow growing alumina scale formed on material surface at high temperature, accompanied by extremely low electrical conductivity (Quadakkers et al, 2003). The second type of potential oxide is silica. However, large amounts of silicon are needed to form stable silica scale which leads to embrittlement (Quadakkers et al, 2003). Therefore, chromium alloys are the only suitable candidates. Although chromia provides less oxidation protection, its electrical conductivity is orders of magnitude larger than alumina and silica (Huang et al, 2000).

In this project, two kinds of alloys were tested: ferritic stainless steel UNS430 (16% ~ 18% chromium) and chromium-based alloy (95% chromium + 5% iron). A critical concentration of chromium is needed to form the protective oxide scale (Shaigan et al, 2008). The ferritic stainless steel is regarded as the most promising material for the interconnect due to its low cost as well as excellent machinability (Visco et al, 2003). In addition, this alloy also has close thermal expansion with other cell components (Chen et al, 2005). An alternative material proposed for the interconnect is a Cr-5Fe alloy. The advantage of this alloy is that it is not prone to hydrogen embrittlement damage at the anode side in contact with the hydrogen environment.

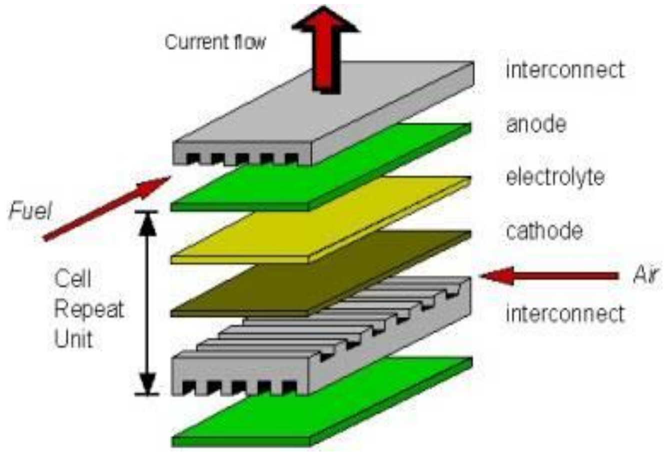

Figure 2.2 SOFC working components (Craig Fisher, 2012)

2.3 Problems of Chromium-based Interconnect

Although chromium-containing alloys are the leading candidates for use as interconnects of fuel cells, they have two main disadvantages that cannot be neglected.

The first is the growth of chromia (Cr_2O_3) scale that contributes to high resistance in the cell stack. The thermally grown oxide scale has poor adhesion when it reaches a higher thickness and is possible to crack and spall during SOFC thermal cycles (Shaigan et al, 2008). The chromia scale forms and grows primarily by outward diffusion of chromium. At the outer surface, oxygen fills oxygen vacancies and forms new oxide. Similarly, chromium vacancies are filled by chromium diffusing from substrate alloy to the scale surface. Thus, the growing chromia scale will continuously create porosity at the alloy/scale interface which may lead to poor adhesion to the substrate. Also, oxygen can diffuse inward through high diffusion paths such as grain boundaries (Fergus, 2005). The whole reaction can be written as:

$$4Cr_{Cr} + 3O_2 = 2Cr_2O_3 \qquad 2\text{-}5$$

The second problem is chromium poisoning. At SOFC operation temperature, the chromia may react with oxygen at the air electrode side and form volatile six-valent chromium species which are detrimental to the cathode (Asteman et al, 1999). The possible reactions are:

$$2Cr_2O_3 + 3O_2 + 4H_2O \Leftrightarrow 4H_2CrO_4\ (g) \qquad 2\text{-}6$$

$$2Cr_2O_3 + 3O_2 \Leftrightarrow 4CrO_3\ (g) \qquad 2\text{-}7$$

$$2Cr_2O_3 + 3O_2 + 4H_2O \Leftrightarrow 4CrO_2(OH)_2\ (g) \qquad 2\text{-}8$$

The gas species then migrate through the cathode, at deposit on the cathode/electrolyte interface as chromia and other unwanted compounds. The chromium deposition can block the triple phase boundaries (YSZ, LSM and O_2), which are the cathode active sites, and the cell performance decreases proportionately (Jiang et al, 2002)

2.4 Oxidation Kinetics and Spinel Coating

In order to suppress the oxidation of the interconnect and chromium poisoning of the cathode, a protective layer can be applied to the surface of the interconnect on the cathode side. The protective layer is aimed at serving as a barrier to block the outward diffusion of chromium, and also to stop the chromia evaporation under SOFC operating conditions (Yang et al, 2005). Therefore, not only the composition of the diffusion barrier but also the method of deposition is of great importance. The protective layer greatly decreases the interfacial contact area specific resistance (ASR) between the cathode and the interconnect by blocking the continuous growth of the chromia scale, which has relatively low conductivity (Montero et al, 2009). Thus, the materials selected for the protective layer should posses high electrical conductivity as well as low chromium cation diffusivity. Low oxygen ion diffusivity is also desirable (Yang et al, 2005). In addition, the thermal expansion coefficient of the coating materials should match with the substrate alloy. The cost of raw materials and the manufacturing process are also important factors for commercial applications (Montero et al, 2009).

Based on these requirements, dense or at least closed porosity layers are needed. Various materials have been tested as coating materials to suppress chromium outward diffusion, such as reactive element oxides (REO) (Whittle et al, 1980), rare earth perovskites, spinels and MALCrY coatings, but only perovskite oxides and spinel oxides can match the conductivity requirements for the protective layer.

In 2005, Virkar et al (Virkar et al, 2005) proposed a model for oxidation kinetics of the metallic interconnect coated with a protective oxide layer. They suggested that there were two possible limiting cases in oxidation kinetics for coated interconnects. The first is chromia scale growing linearly with time meaning the coating is effectively limiting the oxidation; the other one is parabolic growth with time which indicates the coating is ineffectively suppressing the oxidation kinetics. Virkar et al did a series of experiments of perovskite and spinel coatings on Haynes 230 substrate to study the oxidation kinetics and test the effectiveness of reducing oxidation rates. The results showed that the coated samples all had oxide thickness growing linearly with time at different rates while the uncoated sample exhibited parabolic character. Their conclusion was that if coating is thick enough and transport through the coating is slow, the oxide behavior is linear and the coating is effective; if coating thickness is thin and transport is rapid, the oxide behavior is parabolic and coating is ineffective, shown as Figure 2.3 (Virkar et al, 2005).

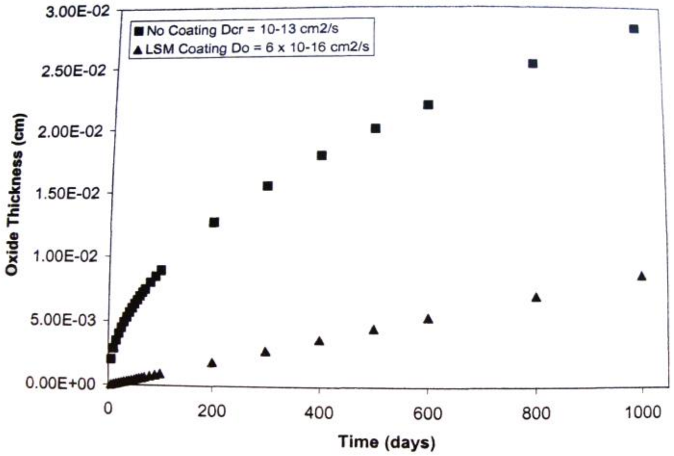

Figure 2.3 Parabolic growing chromia thickness of uncoated sample and linearly growing chromia thickness of LSM coated sample

Perovskites, usually lanthanum-based, have the disadvantage of high cost of both materials and deposition process. Although the oxides have high electrical conductivity as well as high capacity for stopping chromium migration, it is difficult to deposit adherent coatings on the interconnect. On the other hand, spinel oxides are favored for reasons of both good properties and easier deposition.

Spinel has the formula AB_2O_4. It is a cubic close-packed oxygen lattice with 32 O^{2-} per unit cell (Arillo et al, 1997). In the spinel cell, there are two kinds of cation sites, the tetrahedral site, surrounded by four oxygen atoms, just like the diamond structure, and the octahedral site, which has six oxygen atoms around it (Figure 2.4). A and B cations occupy interstitial sites, and the spinel can be represented by $(A_mB_{1-m})_{tetr}(A_{1-m}B_m)_{oct}O_4$, where the number of occupied octahedral sites is always twice that of tetrahedral sites. The inversion parameter is given by the number, m. The relocation of ions can cause a change in lattice parameter or a deformed crystal structure (Bordeneuve et al, 2009). Not every interstitial site is filled. For tetrahedral sites, only 1/8 are occupied while for octahedral, half of the sites are filled. The sites are occupied in an ordered manner. For example, the octahedral sites are alternately occupied; therefore, of the six directions of second nearest neighbor sites, three are occupied and three are empty (assuming oxygen occupies the nearest neighbor site). Then distance between nearest octahedral sites is the same as between oxygen atoms. The distance between occupied octahedral and tetrahedral sites is larger and even larger between tetrahedral neighbors (Petric & Ling, 2006). Although over half of cation sites are unoccupied, the vacancy concentration among oxygen ion sites can be neglected. As such, there is no significant anion conductivity throughout the spinel.

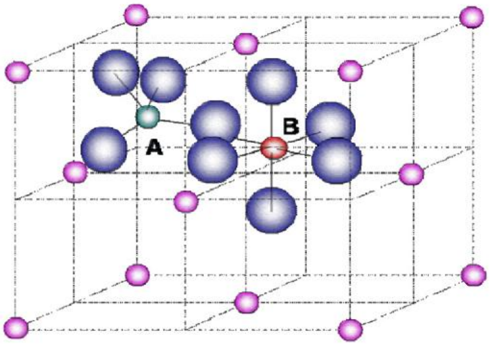

Figure 2.4 Spinel structure and cation distribution

Since the interstices in the spinel structure are filled by two cations, either the same or different, it can accommodate many different metals. Typical transition metals are divalent or trivalent. The tetrahedral site is usually occupied by divalent cationssuch as Mg, Mn, Ni, Zn, Cu or Co, and the octahedral site is usually occupied by trivalent cations such as Al, Cr, Mn, Fe, Co (Qu & Jian, 2005). Although divalent and trivalent ions are common in the spinel structure, quadrivalent cations can also occupy these sites. It is significant to note that some elements such as Mn and Co have multiple valences. They can occupy both tetrahedral and octahedral sites, and this is very useful for spinel electrical conductivity.

Table 2.1 Properties of Transition Metal Spinels (at 800°C Except Where Noted) (Petric & Ling, 2006)

	Mg	Mn	Co	Ni	Cu	Zn
Al	$MgAl_2O_4$ $\sigma = 10^{-6}$ $\alpha = 9.0$	$MnAl_2O_4$ $\sigma = 10^{-3}$ $\alpha = 7.9$	$CoAl_2O_4$ $\sigma = 10^{-5}$ $\alpha = 8.7$	$NiAl_2O_4$ $\sigma = 10^{-4}$ $\alpha = 8.1$	$CuAl_2O_4$ $\sigma = 0.05$ --	$ZnAl_2O_4$ $\sigma = 10^{-6}$ $\alpha = 8.7$
Cr	$MgCr_2O_4$ $\sigma = 0.02$ $\alpha = 7.2$	$Mn_{1.2}Cr_{1.8}O_4$ $\sigma = 0.02$ $\alpha = 6.8$	$CoCr_2O_4$ $\sigma = 7.4$ $\alpha = 7.5$	$NiCr_2O_4$ $\sigma = 0.73$ $\alpha = 7.3$	$CuCr_2O_4$ $\sigma = 0.40$ --	$ZnCr_2O_4$ $\sigma = 0.01$ $\alpha = 7.1$
Mn	$MgMn_2O_4$ $\sigma = 0.97$ $\alpha = 8.7$	Mn_3O_4 $\sigma = 0.1$ $\alpha = 8.8$	$CoMn_2O_4$ $\sigma = 6.4$ $\alpha = 7.0$	$NiMn_2O_4$ $\sigma = 1.4$ $\alpha = 8.5$	$Cu_{1.3}Mn_{1.7}O_4$ $\sigma = 225(750^{\circ}C)$ $\alpha = 12.2$	$ZnMn_2O_4$
Co		$MnCo_2O_4$ $\sigma = 60$ $\alpha = 9.7$	Co_3O_4 $\sigma = 6.7$ $\alpha = 9.3$			

In order to identify the best spinel composition for the interconnect coating, properties of candidates need to be examined. Table 2.1 includes most common spinels with their thermal expansion (α) and electrical conductivity (σ) measured at 800°C, which is a typical operating temperature of SOFC. The thermal expansions range from 6.8 to 12.5 ppm/°C, while it is near 10 for chromium alloy and 11 for ferritic stainless steel, thus some spinels can be formed to match with the thermal expansion of the interconnect. For electrical conductivity, however, they differ from each other significantly. For example, all aluminum-based spinels are too low in conductivity, while the manganese based and cobalt based spinels both have much higher values. From the table above, there are two compounds with superior conductivity: $Cu_{1.3}Mn_{1.7}O_4$ and Co_2MnO_4 with conductivities of 225 S/cm and 60 S/cm respectively. A target for the electrical conductivity of the coating material may be considered above 50 S/cm at SOFC operating temperature, and therefore the two compounds both serve the purpose.

The great difference of conductivity values among different kinds of spinels is due to the mechanism of conduction. It is generally believed that spinels conduct electricity by hopping of electrons between the cation sites (Horita et al, 2005). Therefore the presence of multi-valent octahedral cations contributes to conduction. This explains why aluminum based spinels exhibit low conductivity. Aluminum is uniquely trivalent and also has strong octahedral site preference energy. Conversely, manganate spinel compounds have higher electrical conductivities since manganese has multiple valence states. Generally, manganese is stable as Mn^{2+}, Mn^{3+} and Mn^{4+}. On tetrahedral sites, Mn^{2+} is dominant while on octahedral sites, all valence states are possible. Since Mn^{3+} and Mn^{4+} have stronger octahedral site preference energy (Dorris & Mason, 1987), the conduction is attributed to charge hopping between these two cations (Arun et al, 1997).

Conductivity (σ) is also temperature (T) dependent and can be expressed by the Arrhenius equation, written as (Joffe, 1960):

$$\sigma=\sigma_0 \exp(-E_F /kT) \quad 2\text{-}9$$

where σ_0 is a constant independent of temperature, and E_F is the Fermi level. Thus the conductivity will increase as temperature increases.

2.5 Zn-Mn-O Spinels

Among the spinels listed in Table 2.1, there is very little information about $ZnMn_2O_4$ spinel in the literature to date.

In the 1960s, Toussaint reported the formation of $ZnMn_2O_4$ and $ZnMn_2O_3$ compounds, the latter with cubic symmetry (Toussaint, 1964). In 1965, Driessens and Rieck investigated the equilibria in the Zn-Mn-O system at temperatures between 600°C and 1450°C and for the first time revealed the phase diagram as shown in Figure 2.4 (Driessens & Rieck, 1965). Four phases were observed: a cubic phase α-Mn_2O_3, a tetragonally deformed spinel phase $Zn_xMn_{3-x}O_4$ ($0 \le x \le 1.03$), a cubic spinel phase $Zn_xMn_{3-x}O_4$($0 \le x \le 1.5$) and a zincite phase $Zn_{1-z}Mn_zO$ ($0 \le z < 0.02$). Ninety points were examined over the phase diagram using water quenched samples. The phases were identified by X-ray diffraction. Figure 2.5 shows the points studied by XRD with the Zn-Mn-O system. Pure cubic phase spinel has a broad composition range above 1150°C and only a narrow range as temperature decreases. At zinc-rich compositions, the system is two-phase with cubic spinel and ZnO.

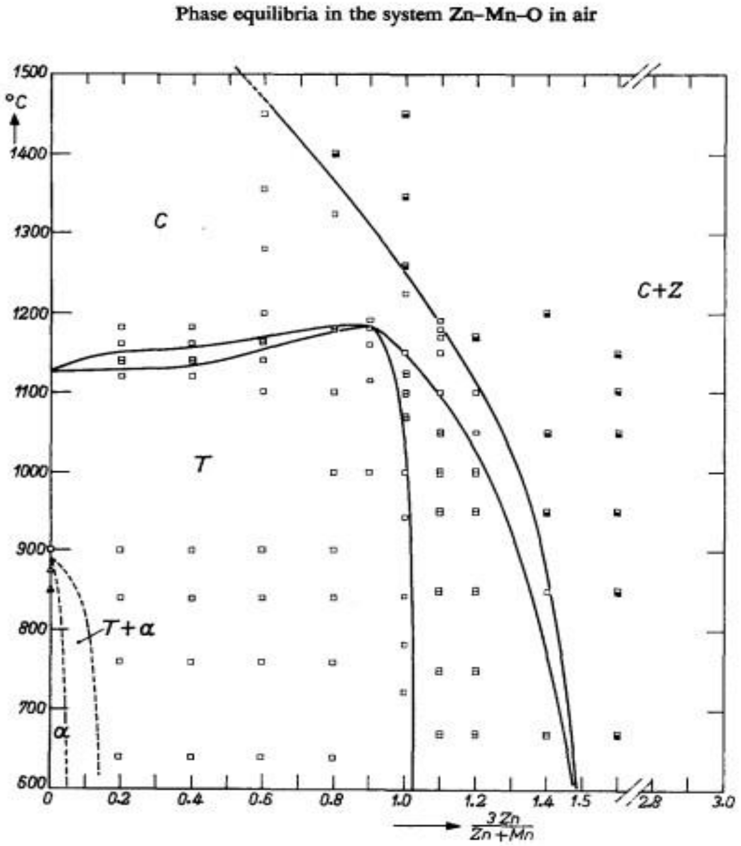

Figure 2.5 Proposed phase diagram for Zn-Mn-O system in air at high temperatures. C represents cubic spinel, T represents tetragonally deformed spinel, α the α-Mn_2O_3 field and Z the ZnO field.

In 2006, Blasco and Garcia re-analyzed the Zn-Mn-O system with a focus on low temperatures, ranging from 450°C to 750°C, and a composition range of $Zn_xMn_{3-x}O_4$ with 1<x<2 (Blasco & Garcia, 2006). Their results (Figure 2.6) showed that a new isolated tetragonal spinel phase at 700°C between x=1.5 and x=1.57. At 600°C, a mixture of two spinels exists between x=1.05 and x=1.55 while the cubic phase is stable only in a narrow range of x = 1.55 to 1.75.

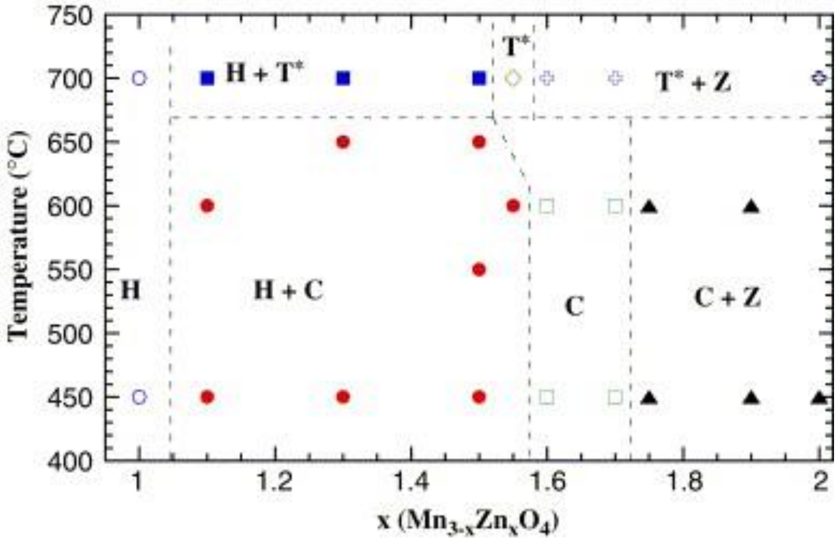

Figure 2.6 Proposed phase diagram for part of the Zn-Mn-O system in air up to 700°C. H, Z, C and T stands for hetareolite, zinctite, cubic spinel and tetragonal spinel phases, respectiviely. T^* indicates that secondary cubic phase is also present and the exact amount depends on the cooling path. (Blasco & Garcia, 2006)

Different results of high temperature were obtained by Peiteado et al (Peiteado et al, 2008). The $Zn_xMn_{3-x}O_4$ spinels have cubic symmetry structure at low temperatures (below 650°C) and distort to tetragonal symmetry as temperature increases. They used nitrogen quenched samples of compositions with x=1, 1.26, 1.41, 1.67 and 2. The phases are shown in Figure 2.7 as a function of temperature and composition based on XRD results.

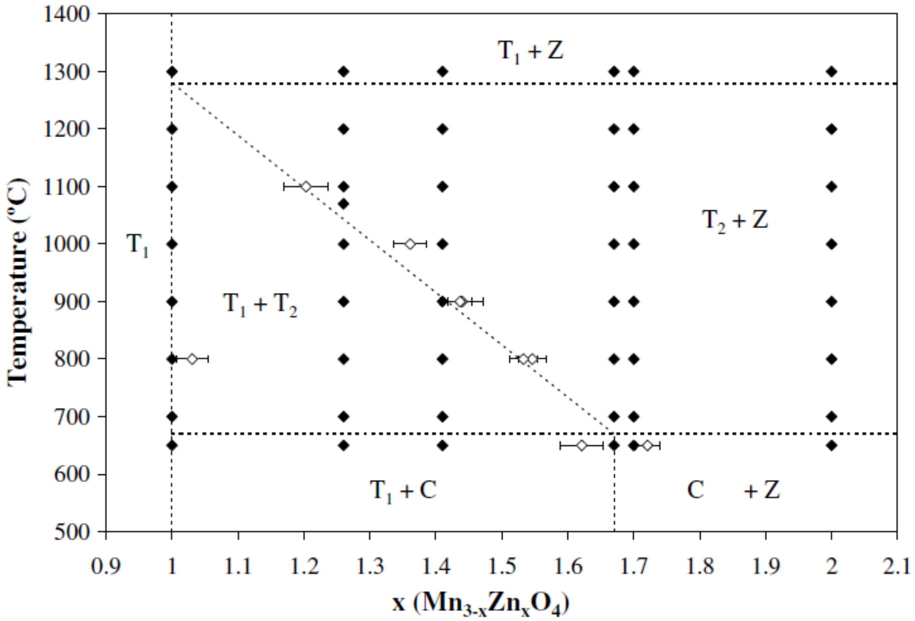

Figure 2.7 Stability regions in the Zn-Mn-O system in air as a function of temperature and composition. C: cubic spinel, T_2: tetragonal spinel, and Z: hexagonal ZnO.

These three researches all used quenched samples for analysis. Quenching is a possible way to freeze in the high temperature structure, but sometimes the kinetic reaction is too fast to do so. This can lead to false results. A more accurate approach is to use high temperature X-ray diffraction.

2.6 Co-Mn-O Spinels

Co-Mn spinels have drawn researchers' attention for a long time since they have high electrical conductivity as well as stable properties and are regarded as the most promising interconnect coating material (Bateni et al, 2006). Figure 2.8

shows the phase diagram of Co-Mn-O system.

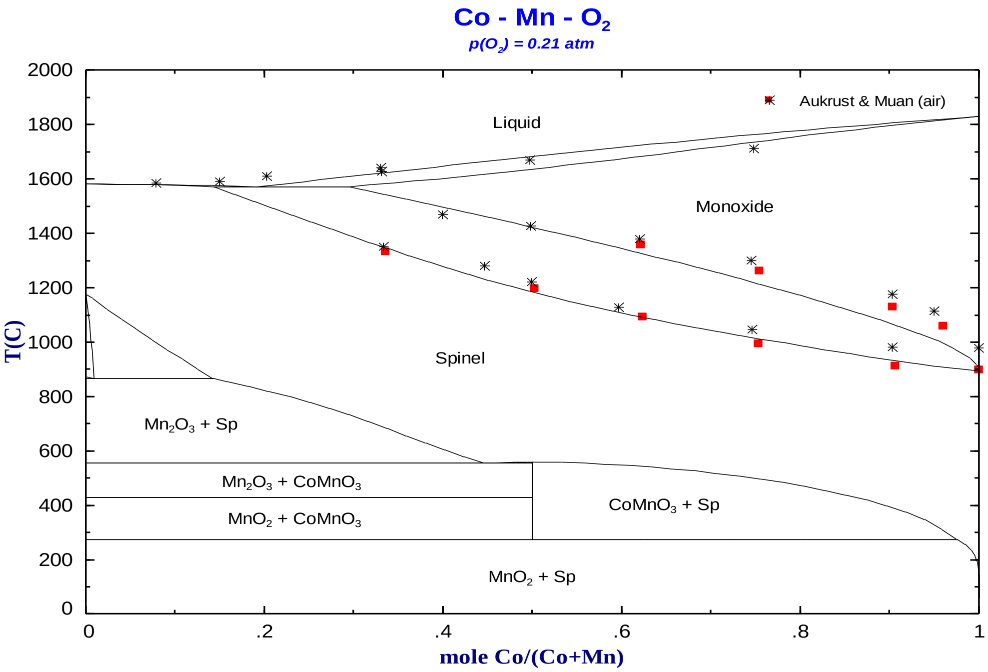

Figure 2.8 Co-Mn-O_2 phase diagram

Manganese based spinels were found to have not only high electrical conductivity but also a large degree of non-stoichiometry. Figure 2.8 shows that the spinel solid solution exists across the whole diagram. At 800°C, the cubic spinel solid solution exists above 25% cobalt. This is very different from how we generally think about stoichiometric compounds that exist as vertical lines in the phase diagram. Although the spinel is written as $CoMn_2O_4$, it actually consists of a range of solid solution.

2.7 Cu-Mn-O Spinels

Cu-Mn spinel has also generated a lot of research interest. Studies show that $Cu_xMn_{3-x}O_4$ spinels have possible use as catalysts for steam reforming of methanol as well as high electrical conductivity. The cation distribution and valence have been investigated. On octahedral sites, not only Mn^{3+}, Mn^{4+} exist, but also Cu^+, Cu^{2+} are present, and this greatly increases the conduction of $Cu_xMn_{3-x}O_4$ spinels. Unlike Co-Mn spinel that has a wide phase stability region, the Cu-Mn-O system shows a limited homogeneity range at the temperature of interest, shown in Figure 2.9. In addition, the Cu-Mn spinels are less stable than Co-Mn spinels due to the higher vapor pressure of copper.

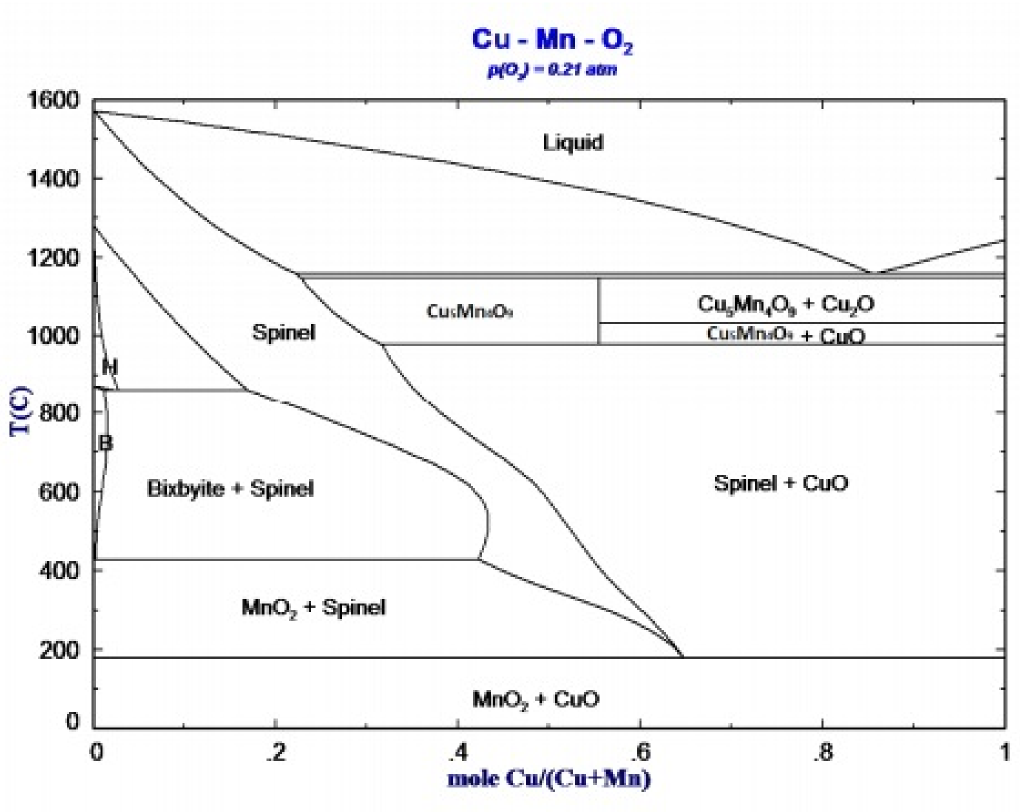

Figure 2.9 Cu-Mn-O_2 phase diagram

Since Co-Mn-O spinels exhibit a wide stability region and Cu-Mn-O spinels exhibit high conductivity, it would be interesting to take advantages of the best properties of the two systems by combining them. Decreasing cobalt content has the advantage of cost reduction and increasing copper should increase the electrical conductivity. In addition, partially replacing cobalt with copper leads to better densification during processing (Montero et al, 2009). Figure 2.10 shows the phase diagram of the Co-Cu-Mn ternary system at 800°C which exhibits a large spinel region in the center.

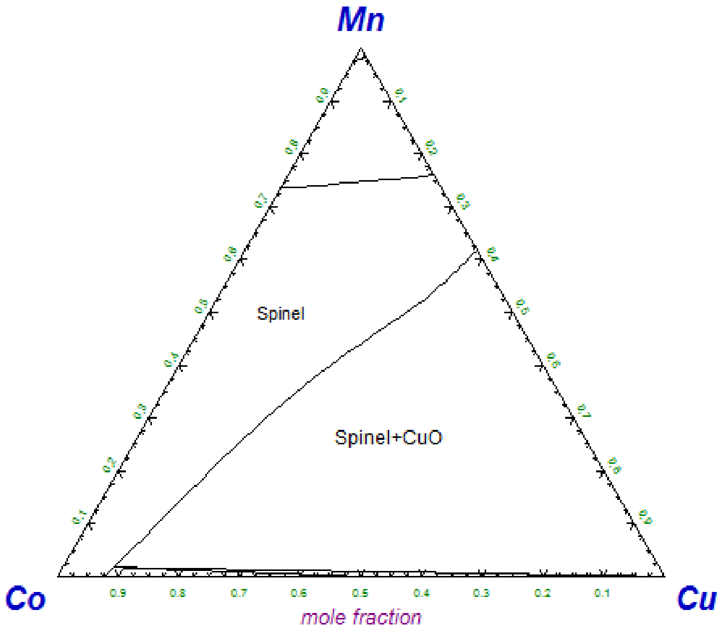

Figure 2.10 Co-Cu-Mn-O_2 phase diagram at 800^{o}C

2.8 Electrodeposition

There are several methods available for depositing the coating onto the interconnect. Slurry coating, screen-printing, physical vapor deposition and plasma spray all have been applied to deposit the coating (Wu et al, 2008). Electroplating of the transition metals followed by oxidizing in air has some distinct advantages (Wu et al, 2007). Electroplating can improve the densification as well as adhesion of coating material in a cost-effective way. In addition, electroplating has less restriction on shape of the substrate, and uniform film can be deposited on patterned substrates. Also, the thickness of the coating layer can be precisely controlled (Wei et al, 2007).

Electrodeposition is a process that transfers ions from an electrolyte solution to deposit onto a conductive cathode by application of electrical current. The electrolyte is a solution containing metal salts. A conductive, clean and chemically active cathode surface is needed in order to obtain a continuous, uniformly grown adherent film. As long as there is a supply of current and enough metal ions in the solution, the deposition can continue, which means a wide range of coating thickness can be applied.

The deposition process is controlled by Faraday's Law, which is described as:

1. The mass of a substance deposited at an electrode during electrolysis is directly proportional to the quantity of electricity transferred at that electrode. Quantity of electricity refers to the quantity of electrical charge, typically measured in coulombs.
2. For a given quantity of D.C electricity (electric charge), the mass of an elemental material transferred at an electrode is directly proportional to the element's equivalent weight.

To express it in a mathematical way, Faraday's laws can be summarized as:

$$m = \left(\frac{Q}{F}\right)\left(\frac{M}{z}\right) \qquad 2\text{-}10$$

where m (g) is the mass liberated at an electrolyte, Q (C) is the total applied electrical charge, F (C/mol) is the Faraday constant which is 96,485 C /mol, M (g/mol) is the molecular weight of substance, z is the valence number of the ion. From Faraday’s law, since M, F and z are all constant, m is proportional to Q.

In order to more clearly understand the control mechanism, Q in Equation 2-10 is replaced by Q=I × t, and thus,

$$m = \left(\frac{I*t}{F}\right)\left(\frac{M}{z}\right) \tag{2-11}$$

where I is applied current and t is for total plating time. Therefore, the amount of deposited substance is directly controlled by plating time at constant current.

One problem in real processing is that the plating efficiency can be decreased by many factors, such as the decomposition of water. Thus the equation should be modified by an efficiency factor η%, written as (Bard & Faulkner, 2001):

$$m = \frac{IM}{Fz}\, t \times \eta\% \tag{2-12}$$

Figure 2.11 shows a simplified electroplating process. The anode serves to complete the circuit by removing the electrons. It needs to be carefully maintained to keep it active, which means no passive film formed on the surface. An active anode is very helpful to replenish the solution from the metal source instead of adding more chemicals. The electrons flow to the cathode surface where metal ions deposit. The reaction can be written as

$$M^{n+} + n\ e^{-} = M \tag{2-13}$$

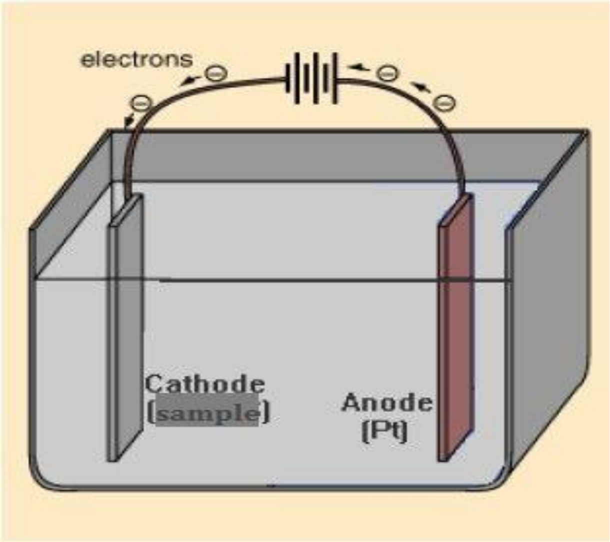

Figure 2.11 Electro-deposition scheme diagram

2.9 Electrode Potentials

During the deposition process, the sequence of metals electroplated needs to be considered, based on the metals' electrode potentials.

The electrode potential, E, is the electromotive force (EMF) of a cell consisting of two electrodes.

$$E_{cell} = E_{cathode} - E_{anode} \tag{2-14}$$

Usually, the cathode side is the electrode potential which is being defined and the anode side is the standard hydrogen electrode (SHE). The SHE forms the basis of thermodynamic scale of potentials. Hydrogen electrode is based on a redox reaction which occurs at the polarized platinum electrode. The electrode is immersed into an acid solution through which hydrogen gas is bubbled. The half cell is

$$2H^{+}(aq) + 2e^{-} = H_2 (g) \qquad 2\text{-}15$$

In order to form an easier comparison with all other elements, the hydrogen standard potential is set to zero at all temperatures. Thus, Equation 2-14 can be rewritten as

$$E_{cell} = E_{cathode} - 0 = E_{electrode} \qquad 2\text{-}16$$

Standard electrode potential is the individual potential of a reversible electrode measured in its standard state, which is 25°C, an effective concentration of 1 mol/L for aqueous species, and a partial pressure of 1 atm of gas reagent. Table 2.2 gives the standard half cell potentials of some common metals including those used in deposition.

Table 2.2 Standard half cell potentials table of common metals

Element	Half cell	Standard potentials(V)
Mn	Mn^{2+} (aq)+ $2e^{-}$ = Mn (s)	-1.18
Zn	Zn^{2+} (aq)+ $2e^{-}$ = Zn (s)	-0.76
Cr	Cr^{3+} (aq)+ $3e^{-}$ = Cr (s)	-0.74
Fe	Fe^{2+} (aq)+ $2e^{-}$ = Fe (s)	-0.41
Co	Co^{2+} (aq)+ $2e^{-}$ = Co (s)	-0.28
Ni	Ni^{2+} (aq)+ $2e^{-}$ = Ni (s)	-0.23
H	$2H^{+}$ (aq)+ $2e^{-}$ = H_2 (g)	0.00

Cu	Cu^{2+} (aq)+ $2e^-$ = Cu (s)	0.34
Ag	Ag^+ (aq) + e^- = Ag (s)	0.80

When the potential is positive, the metal prefers to deposit and remains in the solid state. On the other hand, when the potential is negative, the metal tends to dissolve into the solution. The more noble the standard half cell potentials are, the easier they are to be reduced. For example, Co^{2+} has a standard potential of -0.28 V, and can be reduced by any other electrode whose reduction potential is lower than -0.28 V (e.g., Mn^{2+} = -1.18 V). On the other hand, Co can dissolve in Cu^{2+} solution but remains solid in Mn^{2+} solution. Therefore metals with more noble standard potential should be deposited first.

2.10 Sample Surface Cleaning

The samples can be contaminated during fabrication, cutting or storing. These defects can cause non-adherent, non-uniform or discolored coating (Lowenheim, 1978). Thus, before electrodepositon, the sample surface needs to be carefully cleaned.

Generally there are two main kinds of contaminants.

The first is an oxide layer formed on the surface. Mechanical surface deformation may increase the number of defects, mainly dislocations on the surface. These defects actually provide a quick pathway for chromium outward diffusion, and form a protective oxide film on the surface (Oswald & Grabke, 2004). With this layer, the coating would be difficult to adhere. Manual removal, by grinding with sandpaper is often used to get rid of the oxide film.

The other contaminant is organic dirt, mainly oil and residues from previous sample treatments or operations, for example, the oil used for quenching or fingerprints during working. Such contamination could be cleaned by organic solvents, such as ethanol or acetone.

Based on the surface treatments mentioned above, electropolishing is performed for further surface cleaning. Ostwald and Grabke found that the degree of surface deformation is more or less affected by the extent of oxide formation (Ostwald & Grabke, 2004). Electropolishing seems to be the most efficient method to reduce the oxide growth rate, since this operation can prevent the selectively oxidized elements deep in substrate from diffusing to the surface.

Chapter 3

Experimental Method

3.1 Zn-Mn-O Spinel

3.1.1 Sample Preparation

Nine compositions of $Zn_xMn_{3-x}O_4$ spinel were synthesized by solid-state sintering of oxide powder with x = 0.1, 0.2, 0.6, 0.8, 1.0, 1.2, 1.4, 1.5 and 1.64. ZnO (Alfa Aesar, 99.99% pure) and MnO_2 (Alfa Aesar, 99.9% pure) were carefully weighed based on the molar ratio to obtain a total weight of 20 grams. The powder was then mixed in a 250 mL plastic bottle, which was one third filled with yttria-stabilized zirconia (YSZ) balls as the grinding media. Anhydrous ethanol was added to produce slurry. Next, the powder was ball milled for 24 hours to obtain sufficiently uniform mixing and the resultant slurry was dried in an oven at 80^oC for 5 to 6 hours.

The dried mixed powder was compressed into pellets using a manual press (Model K, F.S. Carver Inc., Summit, NJ, USA), in a round die. The top loading pressure was 10000 pounds and was held for two minutes at a minimum pressure of 7500 pounds. Each pellet was about 2 mm in thickness and 25 mm in diameter. The pellets were heated at 5^{o}C/min to 1200^{o}C and sintered for 24 hours in ambient air. The YSZ balls were cleaned with Ajax cleaning powder followed by sulfuric acid (10%) to prevent contamination for next ball milling.

The fired pellets were water quenched and then crushed and ground into fine powder using an agate mortar and pestle. The ball milling process was repeated to sure dry, well mixed powder.

3.1.2 Conductivity of Rectangular Sample

Before the pressing step, polyvinyl butyral (PVB) binder was added into the powder at 1.5 mL per 10 g powder. PVB was prepared from polyvinyl alcohol by a reaction with butyraldehyde, aimed at increasing the binding strength of the powder to prevent cracks. Stirring was needed to avoid agglomeration. Then the powder was dried and ground, pressed under a force of 15000 pounds in a rectangular die to make conductivity rod samples. Each sample had a dimension about 3.1 × 0.8 × 0.2 cm. The fast heating of the binder can increase porosity and damage during sintering. Thus, the sintering process was set as follows:

1) Increase temperature at a rate of 1^{o}C/min to 450^{o}C and hold for 2 hours;
2) Raise temperature to 690^{o}C at 1.5^{o}C/min and hold for 0.5 hour;
3) Heat to 1100^{o}C at 3.5^{o}C/min and hold for 3 days;
4) Furnace cool.

The slow heating rate prevents explosion of the binder, thus reducing swelling of the pores. At 450^{o}C, the binder was burnt off. Samples were sintered at high temperature in order to promote densification. Furnace cooling, usually at 100^{o}C/h, was used for annealing to avoid inner cracks and residual stress.

3.1.3 XRD Analysis

Before the in-situ high temperature XRD analysis, water quenched samples at specific temperatures were analyzed at room temperature to determine if the samples were fully reacted. This step was performed by decreasing the temperature from 1100^{o}C to the investigation temperature and held for 4 hours, followed by quenching the sample in water. The sintered samples were crushed into fine powder for XRD analysis using Brucker D8 Advanced X-ray powder diffraction with Cu $K\alpha_1$ radiation at 2θ angle ranging from 15^{o} to 80^{o}. The phase was identified by comparison with standards from the Joint Committee on Powder Diffraction Standards (JCPDS) database. If the result showed no raw oxides or a match with the phase diagram, then the reaction was complete.

In-situ high temperature XRD was used to get more precise phase information at various temperatures. This test was performed on a PANalytical X'Pert Pro diffractometer with Cu $K\alpha_1$ $K\alpha_2$ radiations at a 2θ angle range between 15° and 80°. The powder sample was uniformly deposited onto a Pt heater in the Anton Paar HTK 2000 furnace and the temperature was monitored by the thermocouple welded below the Pt heater. The thermal expansion of the Pt heater was accounted for by an automatic temperature-dependent shift of the sample stage. The heating was performed in air. The diffracted X-rays were collected by an X'Celerator detector. For temperatures below 1000°C, the equilibration time for in-situ XRD was 3 to 4 hours whereas for temperatures above 1000°C, the sample was held for 1 to 2 hours. In-situ XRD was performed in both directions (heating and cooling) to confirm that equilibrium was attained.

3.1.4 Electrical Conductivity Measurement

Although the spinel phase has a consistent structure, the electrical conductivity varies with the composition. Conductivity testing was used to optimize the composition. Figure 3.1 shows a schematic diagram of the apparatus used.

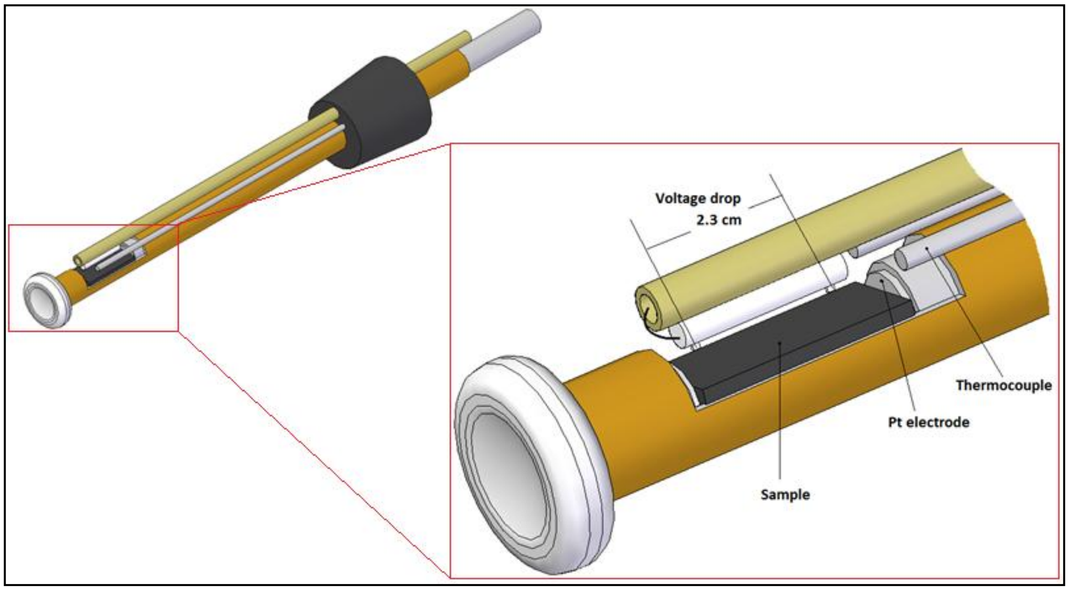

Figure 3.1 Conductivity test apparatus

In this test, the 4–point probe DC method, which is based on the van der Pauw method for measuring electrical resistance by using a 4-point electrical contact was used for measuring electrical conductivity. The rectangular bar sample was slightly polished before testing to get a smooth surface. Platinum paste was applied on the end of the sample to provide a stronger connection with the platinum electrodes. On the top surface, two other electrodes were made to connect to the sample, aimed at measuring the voltage difference between them. Platinum paste was carefully applied to ensure strong bonding between the electrode and the sample to prevent disconnection during the testing. Little platinum paste was applied as during the heating, excess paste would melt and could spread out, thereby decreasing the actual distance between the voltage electrodes.

The sample was inserted into furnace and a thermocouple was placed above the sample. The voltage and temperature electrodes were connected to different multimeters and monitored by LABVIEW^{TM}. Data points were recorded at 5 sec intervals.

The conductivity test was operated at temperatures ranging from 600°C to 900°C. The temperature was increased at a rate of 5°C/min until 600°C and kept overnight in order to reach equilibrium. Readings were recorded every 100°C intervals and each temperature interval was held for at least 1 hour to ensure consistent conductivity reading. Measurements were taken from both heating and cooling directions to ensure equilibrium and consistency of conductivity data. With the data of current (I), voltage (V), distance between voltage electrodes (L) and sample cross-section (A), the conductivity (σ) could be calculated as follows:

$$\sigma=\frac{1}{\rho},\ \rho\ =\ \text{resistivity} \qquad 3\text{-}1$$

According to the definition of resistivity,

$$\rho=\frac{R*A}{L}, \text{ where R resistance and A the area of current flow,}$$

Since $R=\frac{V}{I}$, the equation of conductivity is expressed as:

$$\sigma=\frac{I*L}{V*A} \qquad 3\text{-}2$$

For $Zn_xMn_{3-x}O_4$ spinels, conductivity testing was performed on compositions of $x = 0.1, 0.4, 0.6, 1.0, 1.2$ and 1.4.

3.2 Co-Cu-Mn-O Spinel

3.2.1 Electrical Conductivity Measurement

Figure 3.2 shows the 13 test points selected on the Co-Cu-Mn-O ternary phase diagram at 800°C for conductivity testing.

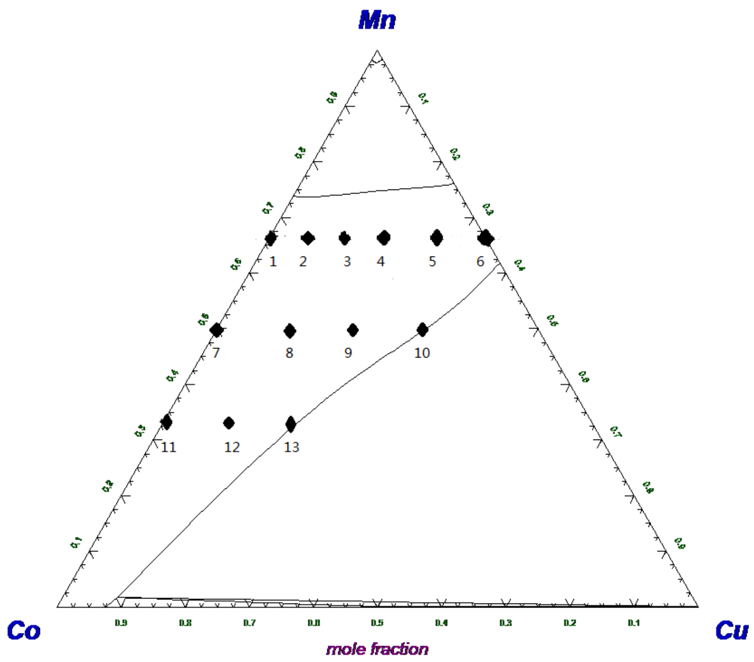
800°C, 0.21 atm O_2

Figure 3.2 Co-Cu-Mn-O phase diagram with tested composition

The same method as used previously for preparing conductivity rod samples was applied for the Cu-Co-Mn-O samples. The raw oxides were Co_3O_4 (Fisher Scientific Company, 99.6% pure), CuO (Alfer Aesar, 99.7% pure) and MnO_2 (Alfer Aesar, 99.9% pure). The sintering process used in this test was as follows:

1) Slowly increase the temperature to 450^oC at a rate of $1^oC/min$ and hold for 2 hours;
2) Raise temperature to 690^oC at $1.5^oC/min$ and hold for 0.5 hour;
3) Heat to 1050^oC at $3.5^oC/min$ and hold for 50 hours;
4) Drop the temperature to 800^oC at a cooling rate of $3.5^oC/min$ to equilibrate the sample.
5) Furnace cool.

3.2.2 Coating Deposition

The coatings were deposited on both stainless steel 430 (from McMaster-Carr) and chromium plate (from Stackpole International) to assess their quality. The coating composition was based on optimal conductivity values obtained from conductivity testing.

Small test coupons were cut from bulk material to a size of 3.3 cm × 5 cm. The thickness of the stainless steel was 1 mm while the chromium plate was 2 mm.

The coupons were ground by 180 grit SiC sandpaper, followed by 240 and 400 grit, to remove surface contaminants and ultrasonically cleaned in ethanol for 5 min at room temperature. After that, the coupons were masked to a specific test area using consumer grade masking tape (Grand&Toy 99838/9), as shown in Figure 3.3. In order to standardize the test, all the sample test areas were held constant at 5 cm^2 and the circular shape also helped to eliminate the edge effect during deposition.

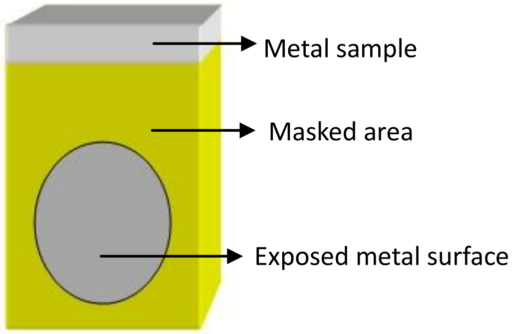

Figure 3.3 Masked small coupon sample

Before metal electroplating, the samples were anodically activated in 10% sulfuric acid for 3 min to remove the oxide layer and guarantee thorough cleaning with a 50 mA/cm^2 current being applied. Then the sample was immediately immersed into the first metal deposit solution. From the EMF values, copper is more noble than cobalt and should be deposited first. However, the experiments showed that copper had poor adhesion to stainless steel and chromium plate, and easily detached during oxidation. Therefore, cobalt was electroplated prior to copper.

The coating method applied was cathodic electrodeposition. Samples were set on the cathode side and connected to the working electrode while the anode was a platinum sheet, connected with counter electrode. Standard saturated calomel chloride was used as the reference electrode and the process was controlled by potentiostant/galvanostat Model 273 (EG&G Princeton Applied Research) and monitored by LABVIEW^{TM}. All electrodes were immersed in deposition solution in a 250 mL beaker. Stirring was essential during electroplating. Figure 3.4 shows a schematic diagram of the deposition apparatus.

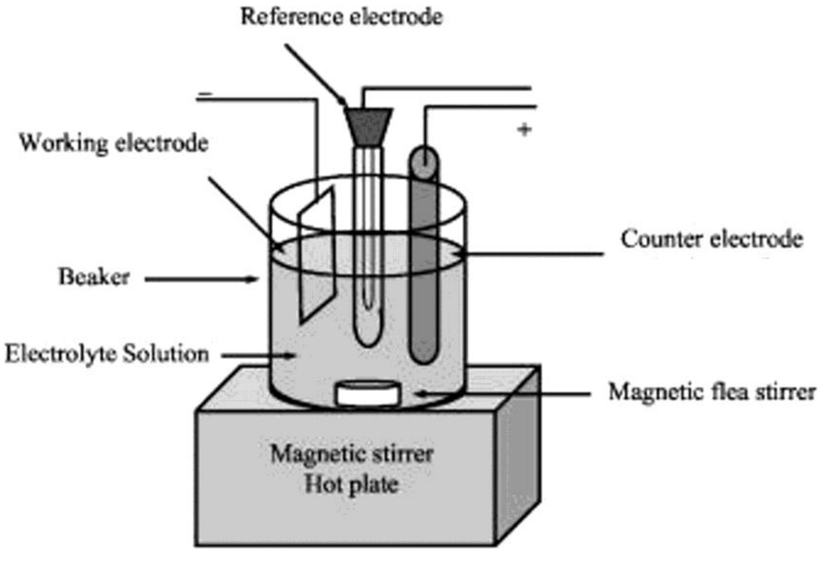

Figure 3.4 Electroplating process apparatus

The cobalt solution consisted of 0.32 mol/L cobalt chloride ($CoCl_2$) and 0.2 mol/L boric acid (H_2BO_3). The starting pH was about 4.2 but as electroplating carried on, the pH gradually dropped. However, within a large range of pH, uniform and thin films could still be deposited. The applied current density was 15 mA/cm^2, and the experiment showed a coating efficiency of 75%, resulting a coated film thickness of approximately 0.24 µm per minute. Upon completion, the current was turned off before the sample was retrieved in order to avoid overload. The sample was rinsed by deionized water before the next deposition.

Since copper is more noble than cobalt, a displacement reaction could occur once the cobalt film was immersed into the copper solution before current was applied causing the final composition to be less accurate. In order to minimize this reaction, the following procedure was developed: 1) before the power was turned on, use a wire with a resistance of 100 Ω to connect anode (platinum plate) and cathode (sample); 2) turn on the power to let current flow; 3) insert the sample and disconnect the wire immediately. The copper solution contained 0.8 mol/L copper sulphate ($CuSO_4$) and 40 g/L of sulphuric acid (H_2SO_4) with a starting pH of 0.65. The applied current density was 48 mA/cm^2 and the coating efficiency could be as high as 99%. Therefore the film would be deposited at 1.05 µm/min. The copper coating process was not sensitive to pH.

Manganese was the last metal to be deposited. The solution contained 0.3 mol/L manganese sulphate ($MnSO_4$), 1.0 mol/L ammonium sulphate ($(NH4)_2SO_4$) and 2 g/L hydroxylamine hydrochloride ($NH_2OH{\cdot}HCl$) with a starting pH of 3.02. Manganese electroplating is very sensitive to pH and had an optimum range of 3.2~2.8. When above or under this range, the manganese would not coat uniformly and would produce defects. The coating efficiency was 50% while applying 100 mA/cm^2 of current density, leading to film thickness deposition 1.15 μm per minute. After cutting off the power, the sample had to be removed from the solution immediately since manganese can dissolve in the solution. A clean napkin or dry air flow was used to dry the sample.

3.2.3 Coating Oxidation

The coated test coupon was the oxidized in the furnace. Several experiments with different heat treatments were designed to discover the optimum oxidation method.

1. The stainless steel coupon sample was deposited with a sequence of Co-Cu-Mn, to a target composition of $Co_{0.5}Cu_{0.5}Mn_2O_4$. The samples were then oxidized in air at a heating rate of 1 ^{o}C/min to 800^{o}C and held for 24 hours and then 120 hours. Samples were cooled down to room temperature at 5 ^{o}C/min.
2. The same deposition method and oxidation method with Experiment 1

was applied on Cr-5Fe coupon samples, also with 24 hours and 120 hours oxidation dwell time.

3. For comparison, a different deposition time was applied on chromium plate and the coating oxidized in air at 800°C for 120 hours, with an expected spinel composition of $Co_{0.5}CuMn_{1.5}O_4$.
4. Chromium plate with a Co-Cu-Mn deposition sequence was oxidized in pure oxygen at 800°C for 120 hours. Before oxidation, the furnace was purged with oxygen (Alphagaz, purity>99.999%) for half an hour. The heating rate was 1 °C/min. The oxygen flow rate was maintained at about one bubble per second, which was monitored by flowing the exit gas through water.
5. Chromium plate with a Co-Cu-Mn deposition sequence was first annealed in hydrogen at 800°C for 24 hours; the regulator was set to 10 psi. Then the furnace was purged with argon (Alphagaz, purity>99.999%) for 10 min to evacuate the residual hydrogen. After turning off the argon cylinder, pure oxygen was applied for oxidation with a dwell time of 96 h.
6. Chromium plate with a Co-Cu-Mn deposition sequence was first annealed in hydrogen at 800°C for 24 hours; the regulator was set to 10 psi. Then the argon gas sparged through water was flowed to the furnace. The water bath heated to about 50°C to increase the water vapor partial pressure. The sample was oxidized in humidified argon for 72 hours.

7. The chromium plate was coated for 30 seconds with cobalt followed by the Cu-Co-Mn electroplating sequence. The sample was first annealed in hydrogen at 800^{o}C for 24 hours and then oxidized in 1% oxygen + 99% argon atmosphere for 24 hours. The first 30-second of cobalt deposition was aimed at providing a better adhesion between the substrate and copper since it was very difficult to electroplate copper onto the chromium plate. The mixing gas of oxygen and argon was calculated and monitored by flow meters (Matheson). The flow meters were calibrated before set up. Both cylinders were opened to 20 psi. The oxygen and argon flow meters were adjusted to the scale reading of 18 and 138, respectively, which correspond to 5.24 SCCM oxygen and 524 SCCM argon.
8. The chromium plate with 30 second of cobalt then the Cu-Co-Mn deposition sequence was first annealed in hydrogen at 800^{o}C for 24 hours, and then oxidized in 1% oxygen + 99% argon. The temperature was first decreased to 600^{o}C at a rate of 5^{o}C/min, held for 10 hours and slowly heated to 800^{o}C at 1^{o}C/min, and held for 24 hours oxidation.
9. The chromium plate with 30 s of cobalt and then followed by Cu-Co-Mn deposition sequence was also annealed in hydrogen at 950^{o}C for 24 hours, then oxidized in 1% oxygen + 99% argon at 800^{o}C oxidation for 24 hours. Increased thickness of coating was also tested in this experiment.

3.2.4 Sources of Experiment Error

Since the 1% oxygen concentration was obtained by mixing pure gases and monitored by flow meters, the degree of uncertainty is quite large. The back pressure on the exhaust gas tubing contributed to an unstable flow of oxygen. The 1% oxygen concentration should be considered as an estimate only.

3.2.5 Coating Analysis

After oxidation, the coating needed to be analyzed to check the validity. This was done by scanning electron microscopy (SEM) coupled with energy-dispersive X-ray spectroscopy (EDS). A small piece was cut from the test coupon, then cold mounted by epoxy (25 grams epoxy resin and 3 grams of hardener). The mounted samples were progressively ground and polished to the grit of 0.05 µm by auto polisher. A JEOL JSM-6610 SEM was used to examine the surface. The epoxy surface was coated with a thin layer of carbon to make it conductive but not affecting the EDS result. Silver paste was used to electrically ground the sample to the stage. EDS was performed with an Oxford Instruments X-Max attachment. Elemental distribution was characterized by line scan and mapping, mainly focusing on chromium diffusion.

Chapter 4

Zn-Mn-O Spinel Results

4.1 XRD results

In-situ high temperature x-ray diffraction was used to examined the structure of $Zn_xMn_{3-x}O_4$, x = 0.1, 0.4, 0.6, 1.0, 1.2, 1.4, 1.5 and 1.64, within a range of temperature from 600^oC to 1300^oC. There are four different phases, cubic spinel, tetragonal spinel, manganese sesquioxide and zinc oxide (ZnO) in the Zn-Mn-O system. The cubic spinel phase is stable on the manganese-rich side at high temperatures, and when the temperature decreases, cubic spinel transforms into tetragonal spinel. At zinc-rich compositions, the cubic phase and zinc oxide phase co-exist. Figure 4.1 gives detailed XRD results of $Zn_{0.1}Mn_{2.9}O_4$. Similar results were obtained from all other compositions (Appendix B). The bottom spectrum in each figure corresponds to the peaks of platinum.

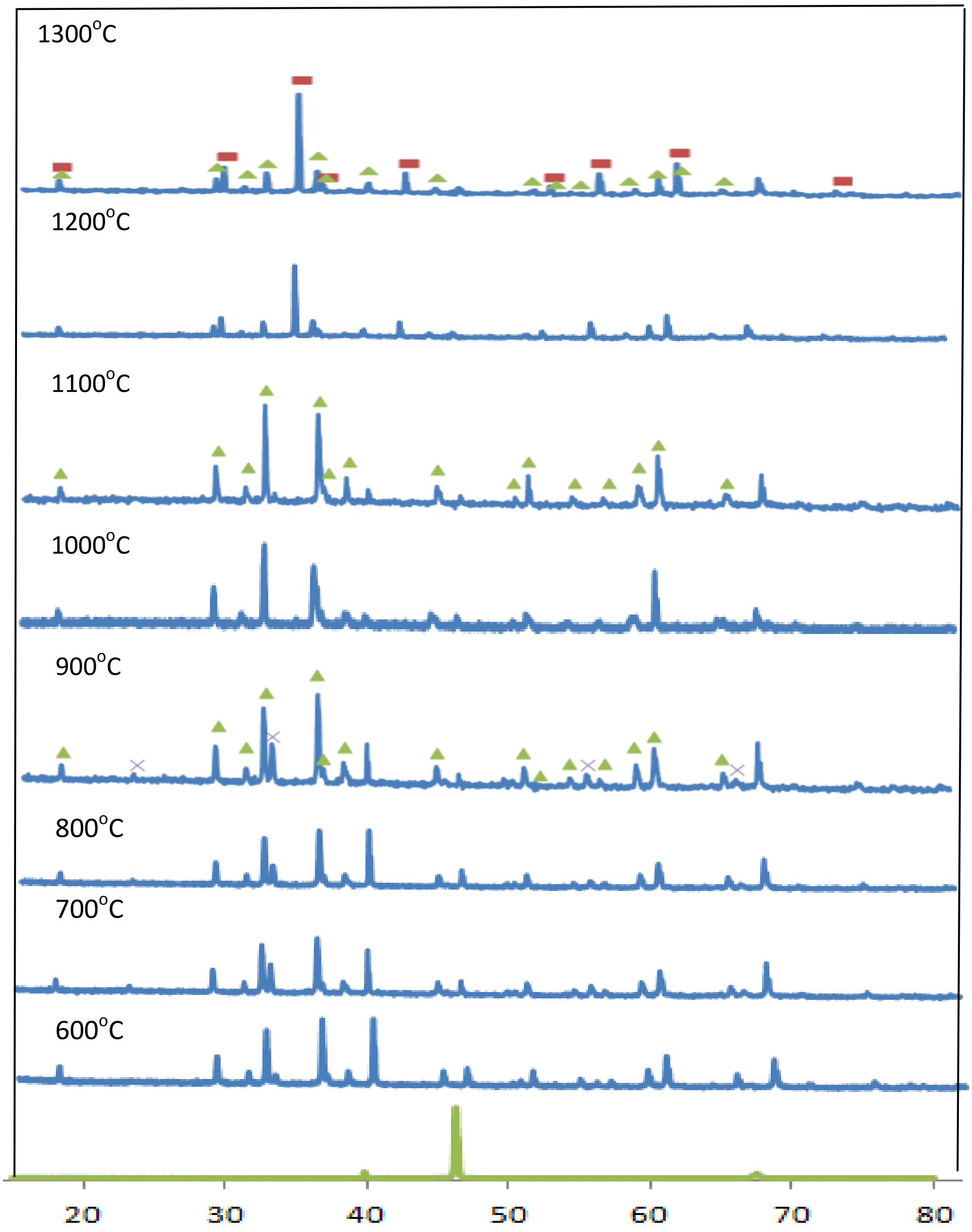

Figure 4.1 XRD results of $Zn_{0.1}Mn_{2.9}O_4$. 1300°C-1200°C, C+T; 1100°C-1000°C, T; 900°C-600°C, T+Mn_2O_3. 🟥 cubic ▲ tetragonal × Mn2O3

Based on the in situ high temperature XRD results, a phase diagram can be constructed as shown in Figure 4.2.

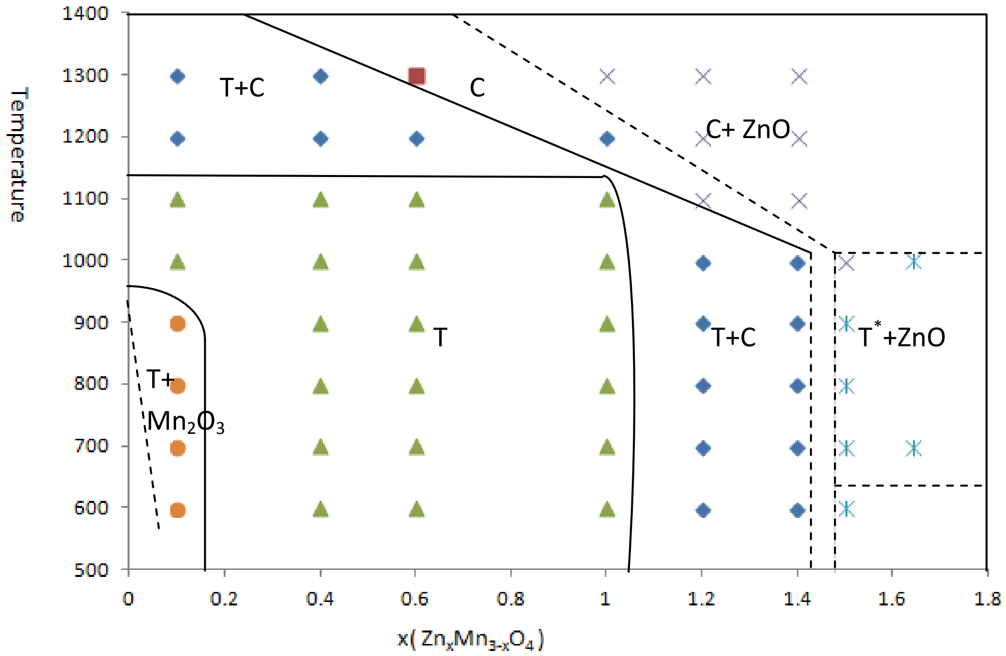

Figure 4.2 Tentative binary phase diagram of Zn-Mn-O spinel. T is tetragonal spinel, C is cubic spinel, T^* is tetragonal with a secondary cubic phase. The dotted line refers to uncertain phase boundary.

Only one point of pure cubic phase was found corresponding to the composition of $Zn_{0.6}Mn_{2.4}O_4$ at 1300°C. The XRD pattern for this point is shown in Figure 4.3. All peaks match the [hkl] values, supporting the existence of cubic spinel phase.

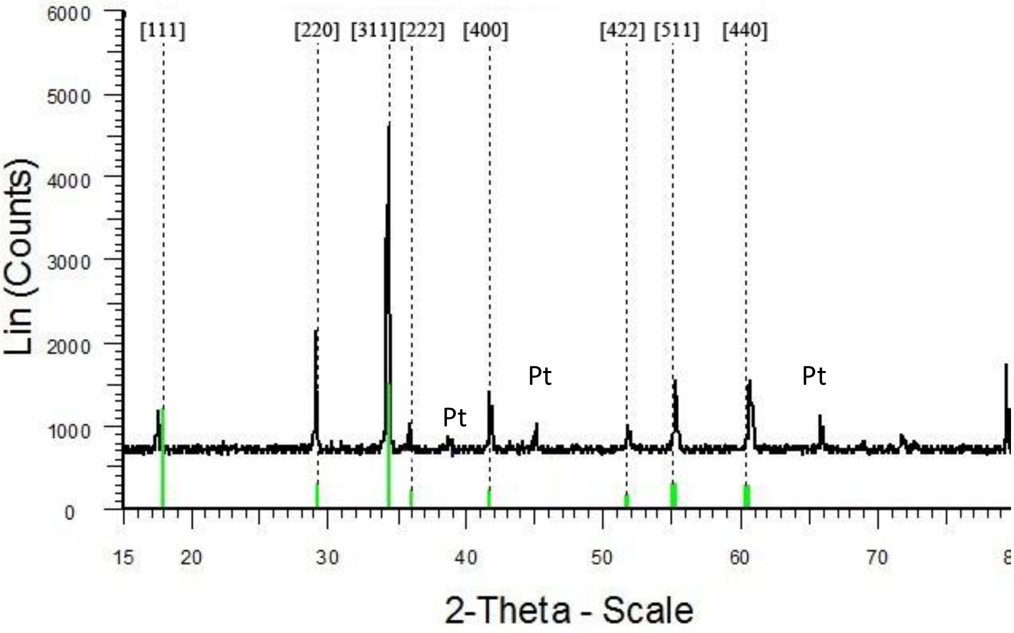

Figure 4.3 XRD results of $Zn_{0.6}Mn_{2.4}O_4$ at 1300°C. The peaks with dotted lines refer to cubic phase while the other peaks belong to platinum.

When temperature decreases, cubic spinel deforms to a tetragonal hetaerolite structure. No cubic phase was detected below 1200°C for $x < 1$ in $Zn_xMn_{3-x}O_4$. A two-phase system composed of cubic and tetragonal shows up as the zinc content increases to a range of $1 < x < 1.5$.

At zinc-rich compositions ($x > 1.5$), the amount of zinc oxide increases at the expense of the cubic phase. For the composition $Zn_{1.5}Mn_{1.5}O_4$ at 600°C to 900°C and $Zn_{1.64}Mn_{1.36}O_4$ at 700°C, three phases, tetragonal, cubic and zinc oxide coexist, as is shown in Figure 4.4.

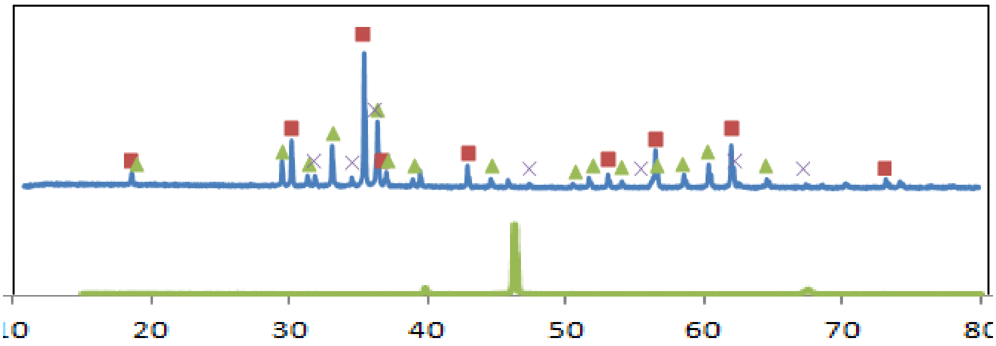

Figure 4.4 XRD results of $Zn_{1.5}Mn_{1.5}O_4$ at 600°C to 900°C.

The Gibbs phase rule states that in thermodynamic equilibrium, which contains P phases and C components, the number of degrees of freedom will be

$$F = C - P + 2 \tag{4-1}$$

The two extra variables refer to temperature and pressure. In the Zn-Mn-O system, pressure is 1 atm and has very little effect on the phase boundaries of condensed phases. Thus Equation 4-1 would be written as $F = C - P + 1$ and the number of components is 3 ($C = 3$). In practice, the oxygen content in the sample equilibrates with oxygen partial pressure at the given temperature. Thus, the equilibrated system can be described in a pseudo-binary phase diagram with $C = 2$ and the Gibbs phase rule will be $F = 3 - P$.

In the case of Figure 4.4, in which three solid phases plus the gas phase exist, greater than the number allowed by the Gibbs phase rule, there are two possible explanations. The first is the temperature is near the upper or lower stability limit of one of the phases (Paulsen & Dahn, 1999) or the composition is located just at the boundary of two fields; the other is incomplete phase transformation due to kinetic reasons. Thus it is possible to have a phase transformation temperature around 600°C at which tetragonal spinel transforms to the cubic phase. This inference is reiterated by Blasco et al. in the low temperature investigation (Blasco & Garcia, 2006).

Unlike the previous research that suggested the presence of a second tetragonal phase (Blasco & Garcia, 2006; Peiteado et al, 2008), there is no composition showing a mixture of two kinds of tetragonal spinels in the high temperature XRD data.

However, a different analysis was captured in a water quenched sample with the composition $Zn_{1.5}Mn_{1.5}O_4$; Figure 4.5 shows the result.

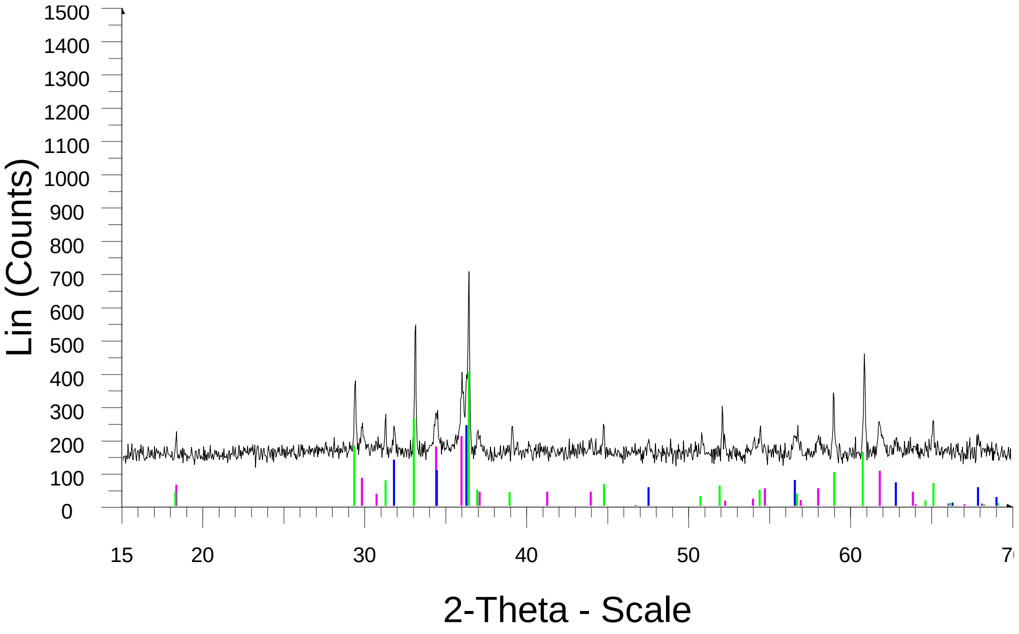

Figure 4.5 XRD result of water quenched sample of $Zn_{1.5}Mn_{1.5}O_4$ from 900°C. Two kinds of tetragonal phases (green and purple) with zinc oxide (blue) were detected.

Two different tetragonal phases in addition to zinc oxide were detected in the water quenched sample, which is different from the result of in situ high temperature XRD (cubic + tetragonal + zinc oxide). The new tetragonal phase has hausmannite structure with a smaller c/a lattice parameter ratio compared with hetaerolite spinel. This phase is what Blasco et al. and Peiteado et al. discovered in their research. They also inferred that this tetragonal phase is deformed variant of the cubic spinel. This inference reasonably explains the difference between the regular XRD patterns of the water quenched sample and the in situ high temperature XRD result. The presence of the new tetragonal phase could be due to the small amount of secondary cubic phase deforming very fast to hausmannite when the temperature decreases, and water quenching method is not fast enough to prevent this transformation from proceeding. Therefore, the high temperature XRD results are more reliable.

However, a complete phase diagram still cannot be constructed, and more research is needed to determine the exact phase boundaries and phase transformation temperatures.

4.2 Electrical Conductivity

Conductivity tests were performed on six compositions, $Zn_{0.1}Mn_{2.9}O_4$,

$Zn_{0.4}Mn_{2.6}O_4$, $Zn_{0.6}Mn_{2.4}O_4$, $ZnMn_2O_4$, $Zn_{1.2}Mn_{1.8}O_4$ and $Zn_{1.4}Mn_{1.6}O_4$. All samples were tested from 600°C to 900°C, on both cooling and heating directions. The results are shown in Figure 4.6.

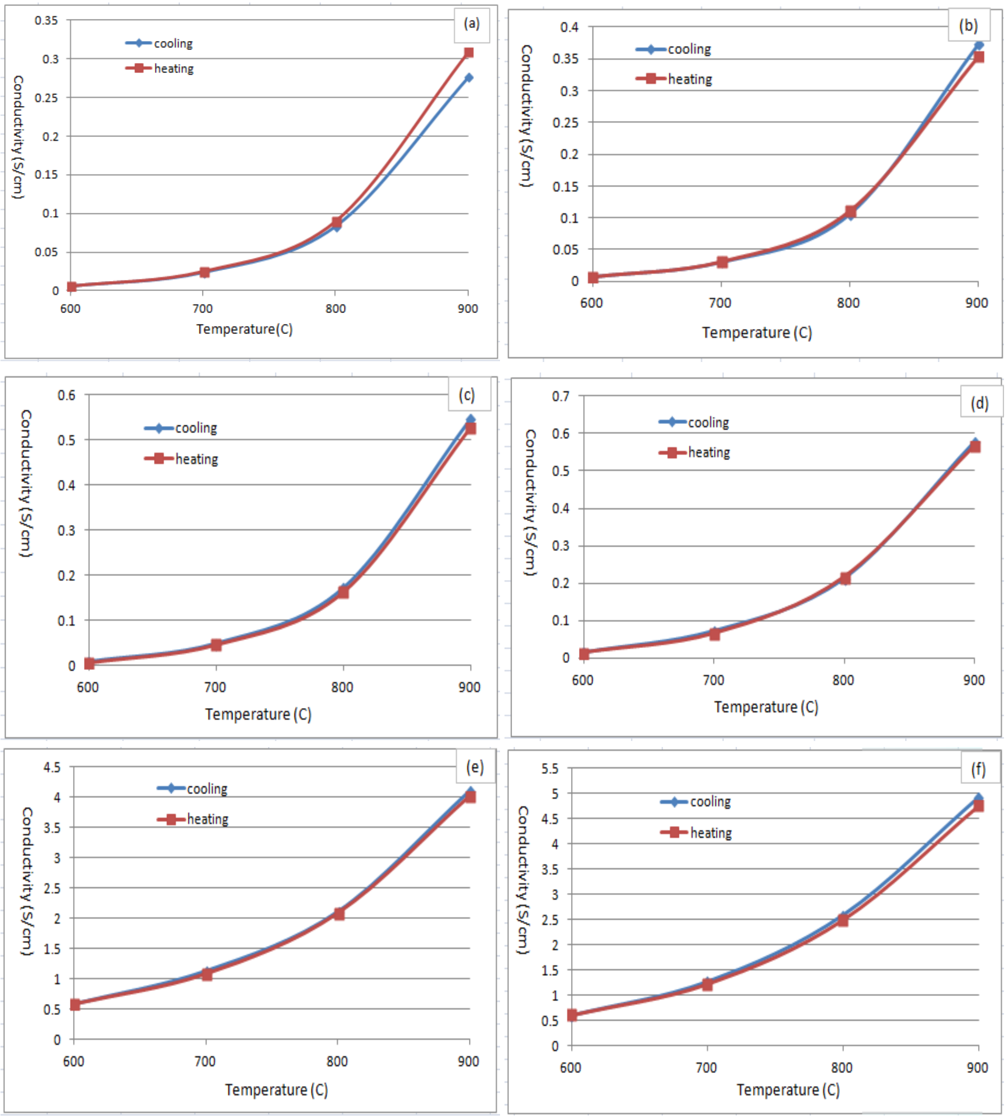

Figure 4.6 Conductivity curves of Zn-Mn-O spinels. (a) $Zn_{0.1}Mn_{2.9}O_4$ (b) $Zn_{0.4}Mn_{2.6}O_4$, (c) $Zn_{0.6}Mn_{2.4}O_4$, (d) $ZnMn_2O_4$, (e) $Zn_{1.2}Mn_{1.8}O_4$, (f) $Zn_{1.4}Mn_{1.6}O_4$

The effect of composition and temperature on conductivity is shown in Figure 4.7. The values are from cooling curves. The electrical conductivity increases as the temperature and the content of zinc increase; there is a dramatic increase between $ZnMn_2O_4$ and $Zn_{1.2}Mn_{1.8}O_4$ where the phase transformation happens, which indicates the cubic structure is much more conductive than the tetragonal structure.

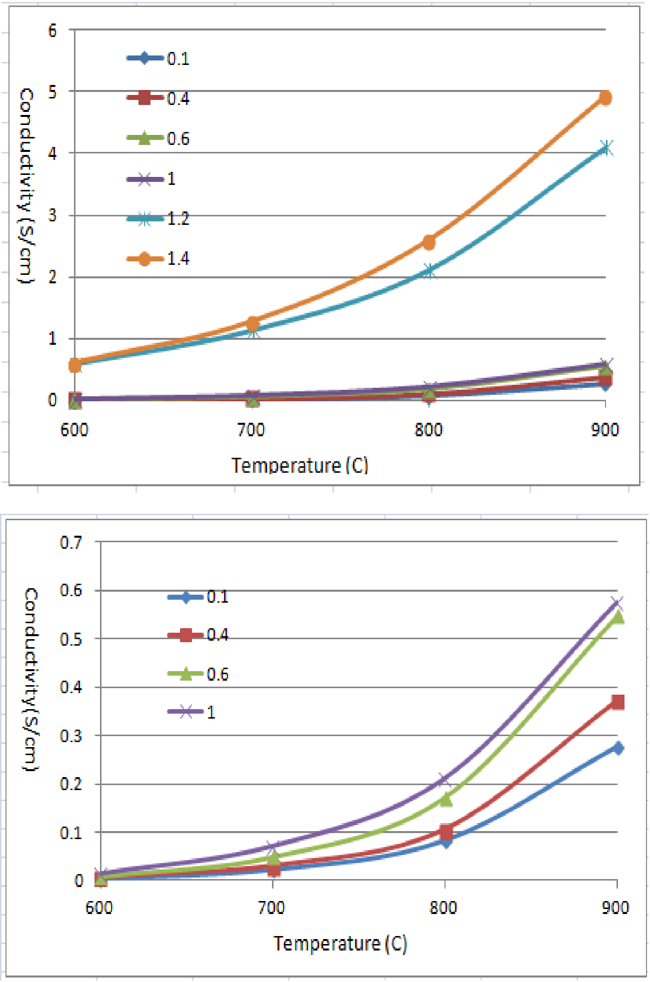

Figure 4.7 Effect of composition and temperature on conductivity

From the cooling curve values, ln(conductivity) vs. 1/T (1/K) can be plotted as Figure 4.8.

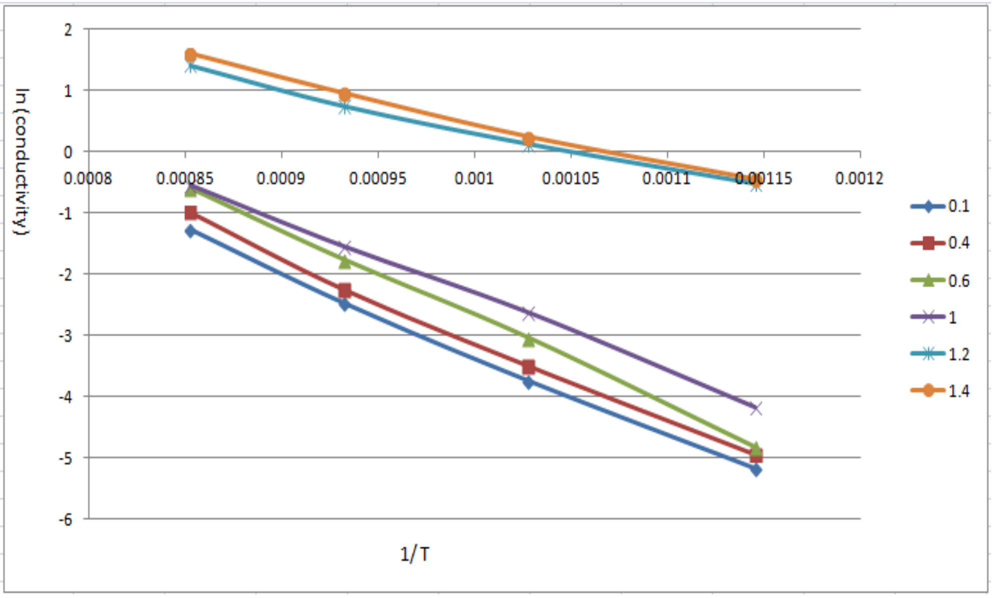

Figure 4.8 Linear relationship between ln(conductivity) and inverse temperature

All plotted results give a linear relationship between ln(conductivity) and 1/T, which confirms Equation 2-9. Equation 2-9 can be rewritten as:

$$\ln(\sigma) = \ln(\sigma_o) - \frac{E_F}{k}\left(\frac{1}{T}\right) \qquad 4\text{-}1$$

Thus, the slope of each plot is $-(\frac{E_F}{k})$, and the intercept is the pre-exponential constant. Both E_F and σ_o can be calculated from the plots. If k is replaced by R in the equation, the active energy E_a can be calculated by replacing E_F. The results are given in Table 4.1.

Table 4.1 Fermi level and pre-exponential constant for each composition

Composition	E_F (×10^{-19} J)	σ_o (×10^4 S/cm)	E_a (×10^4J/mol)
$Zn_{0.1}Mn_{2.9}O_4$	1.83	2.07	11.01
$Zn_{0.4}Mn_{2.6}O_4$	1.85	3.10	11.14
$Zn_{0.6}Mn_{2.4}O_4$	1.98	7.06	11.92
$ZnMn_2O_4$	1.70	2.02	10.23
$Zn_{1.2}Mn_{1.8}O_4$	0.90	0.10	5.42
$Zn_{1.4}Mn_{1.6}O_4$	0.96	0.18	5.78

Based on XRD measurements, the cell lattice dimensions also change with composition. Table 4.2 gives information on cell distortion ((c - a)/a) and cell volume (c × a^2) at 700°C for different compositions.

Table 4.2 Cell distortion and volume of different compositions

Composition	(c - a)/a	Volume(Å^3)	Phase	σ(S/cm)
$Zn_{0.4}Mn_{2.6}O_4$	0.639	322.56	T	0.030
$Zn_{0.6}Mn_{2.4}O_4$	0.626	320.86	T	0.048
$ZnMn_2O_4$	0.595	314.44	T	0.072
$Zn_{1.2}Mn_{1.8}O_4$	0.616	312.37	T+C	1.13
$Zn_{1.4}Mn_{1.6}O_4$	0.616	310.25	T+C	1.27

In the tetragonal spinel phase region, as conductivity increases, the cell distortion and the cell volume both decrease; in the two phase (tetragonal and cubic) region, however, the cell distortion remains constant but cell volume decreases. The decrease of cell volume is proportional to the increase of zinc content, as is shown in Figure 4.9.

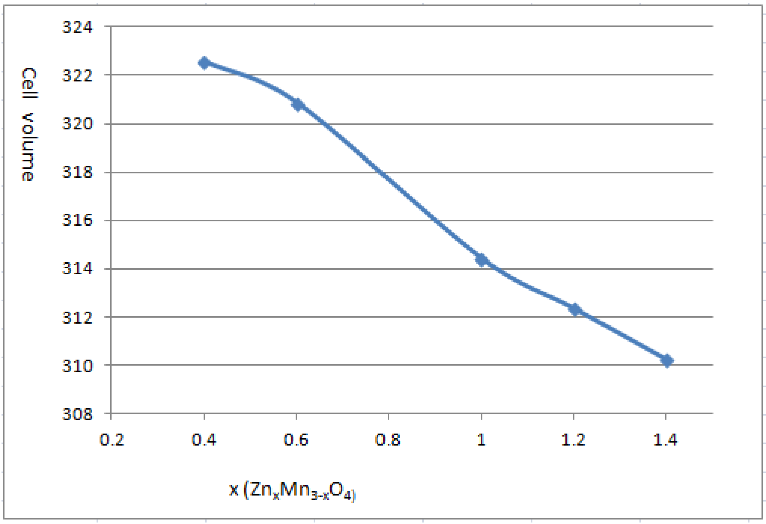

Figure 4.9 Cell volume of $Zn_xMn_{3-x}O_4$ as a function of x

Since conductivity is controlled by electron hopping between octahedral sites, the shorter the hopping distance or the higher the temperature, the greater the frequency and the faster charge will move, which will lead to higher electrical conductivity. A smaller cell volume implies a shorter hopping distance and thus an increase in conductivity.

At 800°C, no pure cubic phase was detected for any compositions in the Zn-Mn-O system and the conductivities were too low to be considered for the interconnect coating. Therefore, another system, Co-Cu-Mn-O was investigated.

Chapter 5

Co-Cu-Mn-O Spinel

5.1 Electrical Conductivity

Co-Cu-Mn-O spinel electrical conductivity was measured for thirteen different compositions within the spinel phase. The temperatures tested were 600°C to 850°C, in both cooling and heating directions. The results are shown in Figure 5.1.

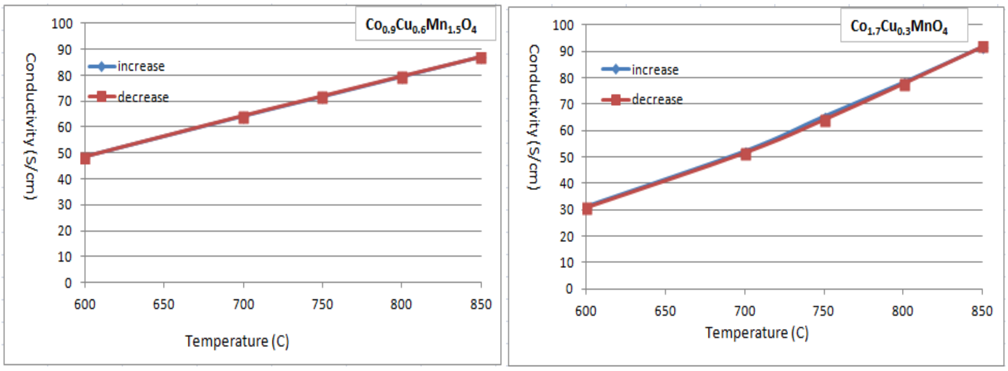

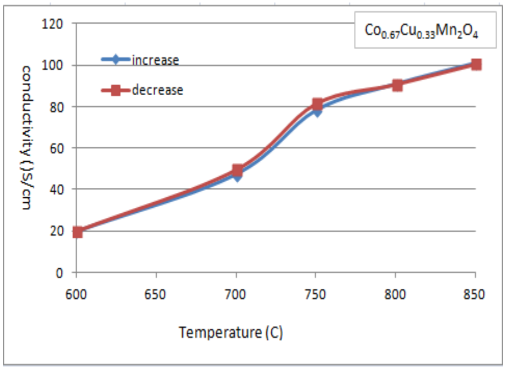
$Co_{0.67}Cu_{0.33}Mn_2O_4$
increase
decrease
conductivity (S/cm)
0
20
40
60
80
100
120
600
650
700
750
800
850
Temperature (C)

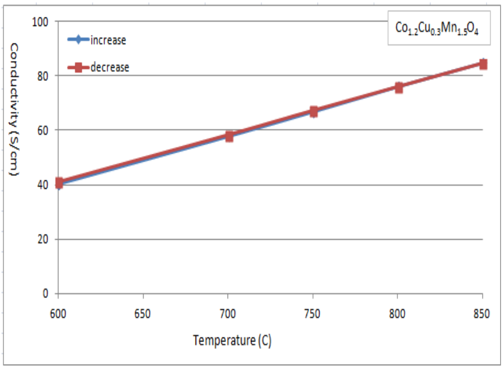
$Co_{1.2}Cu_{0.3}Mn_{1.5}O_4$
increase
decrease
Conductivity (S/cm)
0
20
40
60
80
100
600
650
700
750
800
850
Temperature (C)

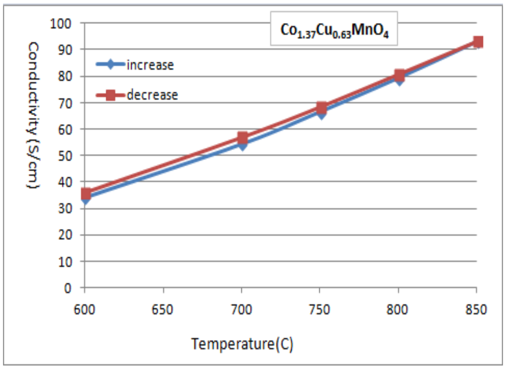
$Co_{1.37}Cu_{0.63}MnO_4$
increase
decrease
Conductivity (S/cm)
0
10
20
30
40
50
60
70
80
90
100
600
650
700
750
800
850
Temperature(C)

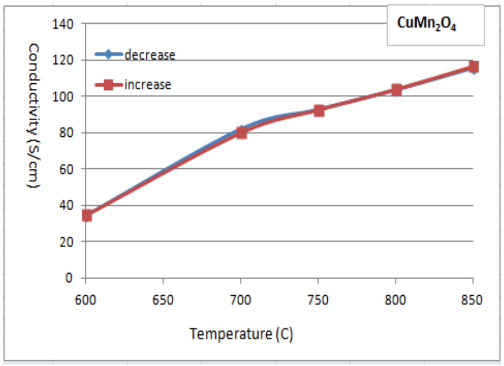
$CuMn_2O_4$
decrease
increase
Conductivity (S/cm)
0
20
40
60
80
100
120
140
600
650
700
750
800
850
Temperature (C)

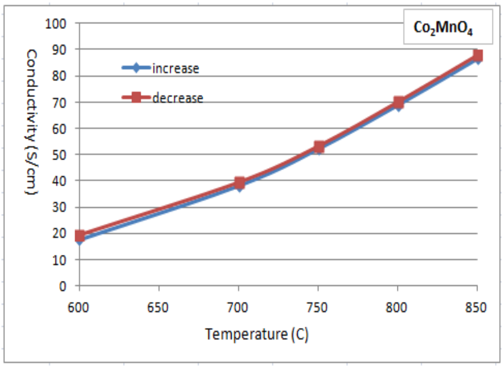
Co_2MnO_4
increase
decrease
Conductivity (S/cm)
0
10
20
30
40
50
60
70
80
90
100
600
650
700
750
800
850
Temperature (C)

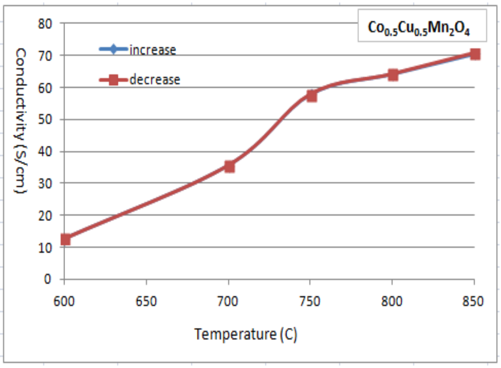
$Co_{0.5}Cu_{0.5}Mn_2O_4$
increase
decrease
Conductivity (S/cm)
0
10
20
30
40
50
60
70
80
600
650
700
750
800
850
Temperature (C)

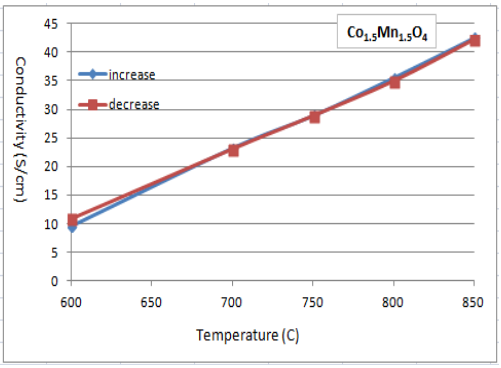
$Co_{1.5}Mn_{1.5}O_4$
increase
decrease
Conductivity (S/cm)
0
5
10
15
20
25
30
35
40
45
600
650
700
750
800
850
Temperature (C)

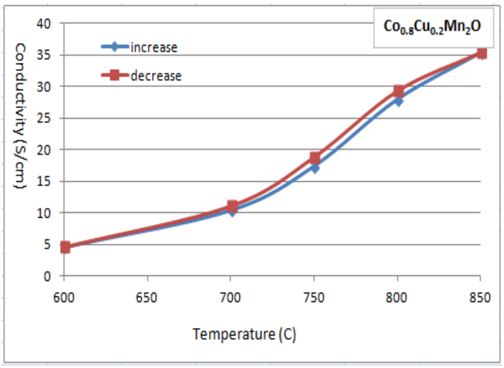
$Co_{0.8}Cu_{0.2}Mn_2O$
increase
decrease
Conductivity (S/cm)
0
5
10
15
20
25
30
35
40
600
650
700
750
800
850
Temperature (C)

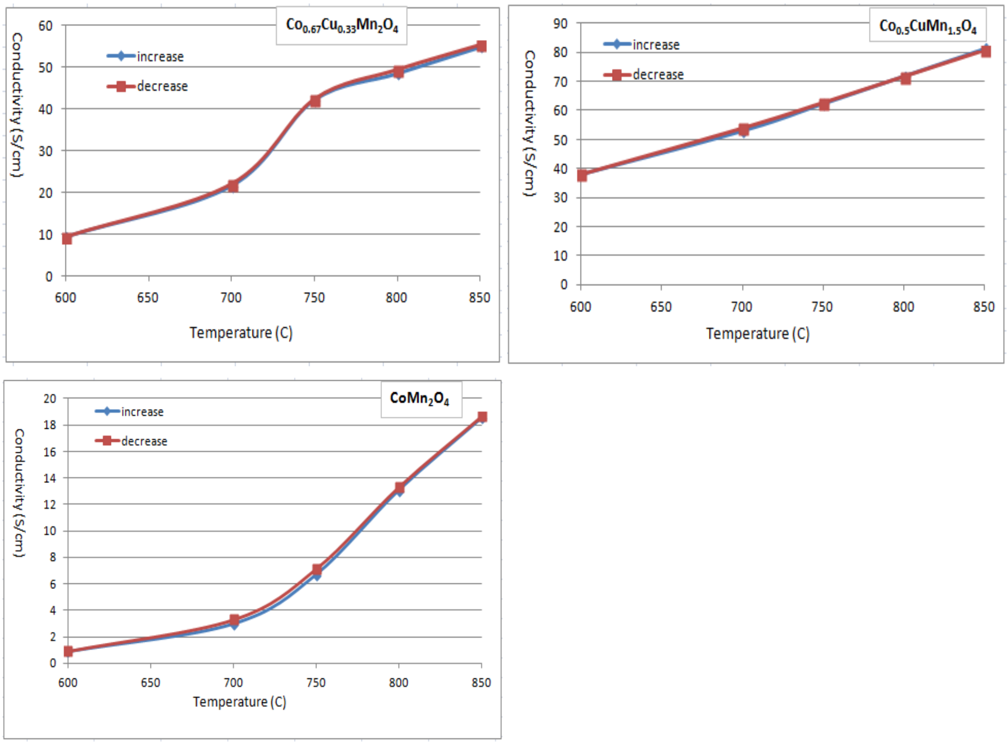

Figure 5.1 Conductivity curves of Co-Cu-Mn-O spinels

These compositions are all spinel structures at 800°C, but as the temperature decreases, phase transformation to a two-phase region will occur for some compositions (e.g., $CoMn_2O_4$), and the conductivity decreases disproportionately. Thus, inflection points observed in the conductivity curves of some samples indicate the phase change.

In order to optimize the composition, a contour map was constructed for better comparison of conductivity (Figure 5.2). Based on the objectives of decreasing the cost and maintaining stability as well as high electrical conductivity of the coating material, the most promising compositions would be within the shaded area. The composition is approximately $Co_{0.5}Cu_{0.5}Mn_2O_4$.

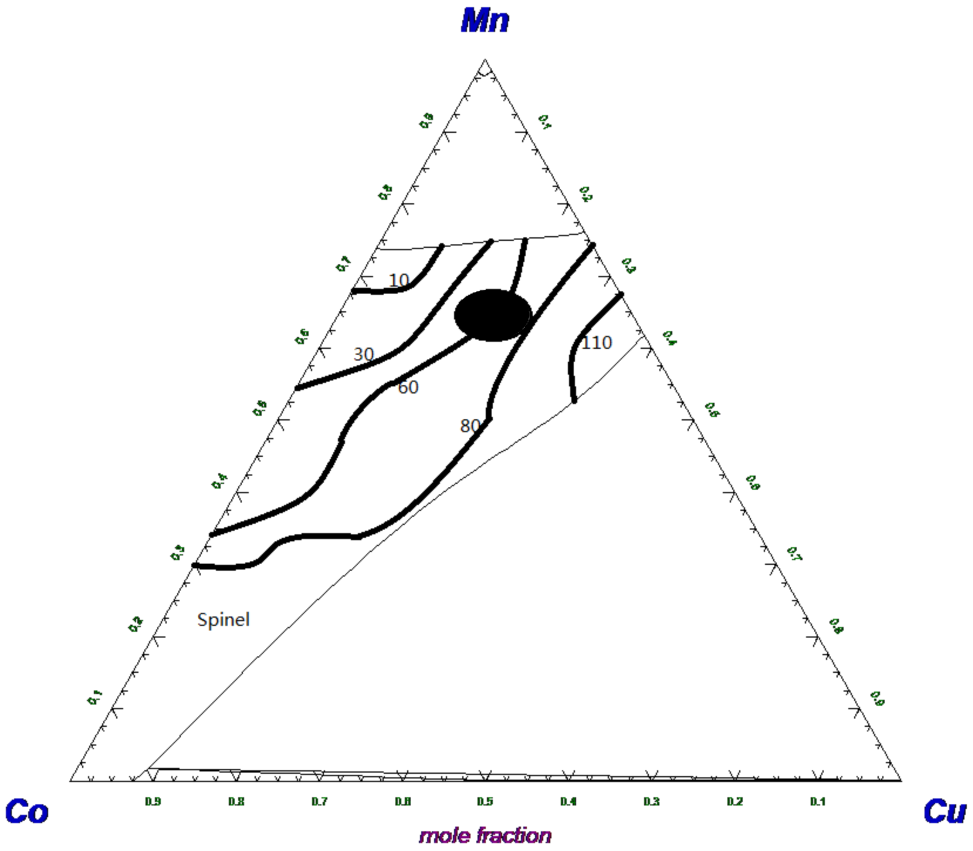

Figure 5.2 Contour map of conductivity for Co-Cu-Mn-O spinel

5.2 Electroplating results

5.2.1 Cobalt Electrodeposition

The plating solution for cobalt electrodeposition consisted of 0.32 mol/L $CoCl_2$ and 0.2 mol/L H_3BO_3. The starting pH was 4.2 and pH decreased with deposition time. The solution yielded strongly adherent coatings on both stainless steel and chromium plate. For the chromium substrate, the cobalt coating sometimes showed non-uniform deposition, as is seen in Figure 5.3.

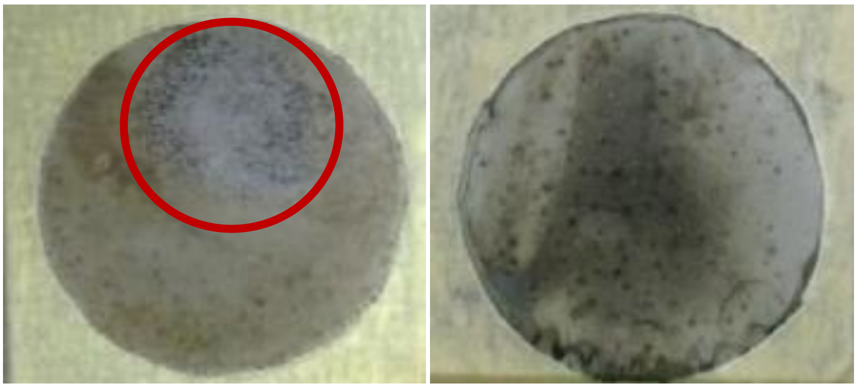

Figure 5.3 Examples of poor outcome of cobalt coating on chromium substrate

The photo on the left shows an area remaining bare without cobalt coating, while the right photo shows uniform coating but has defects visible as black spots distributed over the deposition area. After checking the electroplating parameters including the solution composition and current density, the problem was attributed to surface cleaning. Due to the high chromium content, the polished chromium plate can be rapidly covered with chromia scale, and this scale cannot be removed by dilute acid. Therefore the time between polishing the sample and electroplating should be minimized as much as possible. Figure 5.4 shows a uniform, well-attached cobalt deposition on the chromium plate.

Cobalt electroplating is not sensitive to pH, and well adherent metallic coatings can be deposited even with pH as low as 1.

Figure 5.4 Well-attached, uniform cobalt deposition

5.2.2 Copper Electrodeposition

The solution for copper deposition consisted of 0.8 mol/L $CuSO_4$ and 40 g/L H_2SO_4. A good copper deposition is shown as Figure 5.6. Theoretically, copper should be deposited prior to cobalt since it is more noble, but two problems were observed. The first is that copper can be difficult to deposit on stainless steel and chromium substrates which will lead to decreased coating efficiency. The second problem is the coating will more easily come off after oxidation if electroplating copper first. This may be due to the problem with cleaning the surface or the difference of thermal expansion (TE) between copper and the substrate. The TE values are shown in Table 5.1.

Table 5.1 Thermal expansion coefficient of metals/alloys

Alloys	Cr	Fe	Co	Cu	SS 430
Thermal expansion (ppm/^{o}C)	8	11.7	13.8	16.5	10.45

Copper has 50% higher thermal expansion than the stainless steel. When the sample is being heated, this incompatibility will easily separate the substrate from the copper as well as the whole coating scale, as is shown in Figure 5.5. Cobalt has much closer thermal expansion with steel or chromium and will provide stronger adhesion to the substrate. This explains the better results when cobalt is deposited prior to copper.

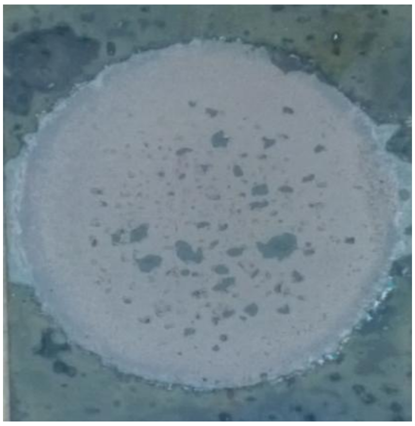

Figure 5.5 Copper spallation during oxidation

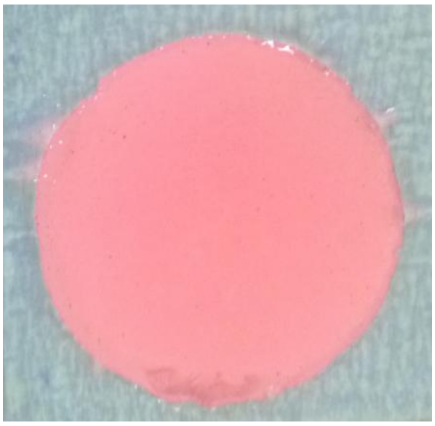

Figure 5.6 Well-attached, uniform electroplating

5.2.3 Manganese Electrodeposition

The last metal in the series to electroplate is manganese and also it is the most difficult process to control. The deposition solution was composed of 0.3 mol/L $MnSO_4$, 1.0 mol/L $(NH_4)_2SO_4$ and 2 g/L $NH_2OH \cdot HCl$. The starting pH was 3.02. Hydroxylamine hydrochloride ($NH_2OH \cdot HCl$) has a very important role during the process. When the deposition begins, manganese oxide (MnO_2) tended to form on the anode surface. Since anode and cathode are in the same solution, precipitates of this oxide would flow to the cathode surface and co-deposit with manganese metal on the sample. This will drastically decrease the efficiency of manganese deposition. These precipitates can be filtered out after each use, but that would be a significant waste of metal. The presence of $NH_2OH{\cdot}HCl$ can greatly reduce this problem. It has been reported that hydroxylamine can work as a reducing agent to prevent oxidation of Mn (II) by dissolved oxygen. (Sylla et al, 2005) Thus, the deposition process will not be affected. However during the experiment, the $NH_2OH{\cdot}HCl$ will be depleted and manganese oxide will recur. Thus after several cycles of deposition, $NH_2OH{\cdot}HCl$ needs to be replenished.

Manganese deposition is very sensitive to pH. As plating time increases, the value of pH will drop quickly. Thus the solution pH needs to be adjusted to 3 by NH_4OH each time. Very high or very low pH will result in non-adherent or non-uniform coating, as is shown in Figure 5.7 and Table 5.2. A good manganese deposition should be uniform in light grey (Figure 5.9).

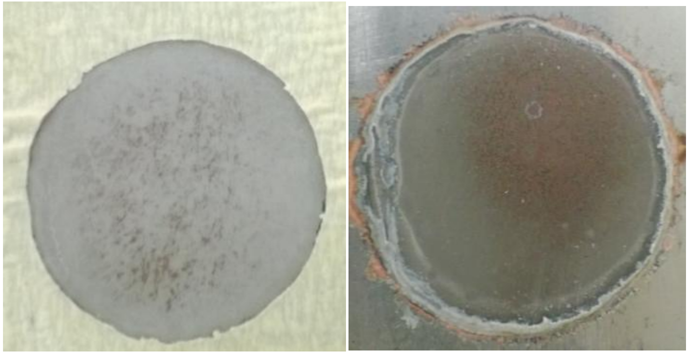

Figure 5.7 Manganese deposition with solution pH=3.4 (left) and solution pH=2.5 (right)

Table 5.2 Manganese deposition in relation to pH of solution

Starting pH	Deposition
3.5	Non-uniform
3.2	Uniform
2.9	Uniform
2.8	Uniform
2.5	Non-uniform

Manganese electroplating is also influenced by the concentration. With very old solution, even if the pH is adjusted, it is still impossible to produce adherent films. The deposition shows a “burnt” surface, as is shown in Figure 5.8. Thus the solution needs to be replenished after several cycles of deposition. The consumption rate of $MnSO_4 \cdot H_2O$ is 0.002628 g/(cm·min) based on Faraday’s Law equation at 100 mA/cm^2 current density.

Figure 5.8 “Burnt” manganese coating with very low concentration solution

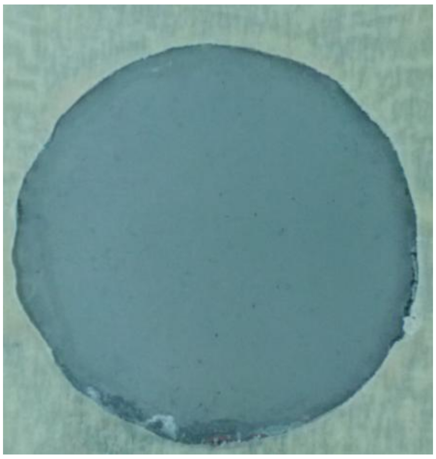

Figure 5.9 Well-attached, uniform manganese deposition

Although the sample was masked to obtain a circular area to avoid edge effect, the deposition is unlikely to be the same thickness over the whole area. Usually the coating near the edge is a little thicker since the deposition progresses from edge to center gradually.

As the final step, the metallic deposit is oxidized to form a spinel phase.

5.3 Oxidation Results

5.3.1 Air Oxidation

5.3.1.1 Coatings On Ferritic Stainless Steel 430

Figure 5.10 shows the SEM cross-section micrograph of $Co_{0.5}Cu_{0.5}Mn_2O_4$ coatings on the stainless steel after 24 hour oxidation. This coating is well adherent with no gaps. There is no obvious chromia scale layer that can be seen. From EDS linescan results, there is an area, shown in the square, rich in chromium, oxygen and other relatively minor metals. Adjacent to the substrate, there is some cobalt and copper (white phase, shown in the circle) forming a solid solution with chromium.

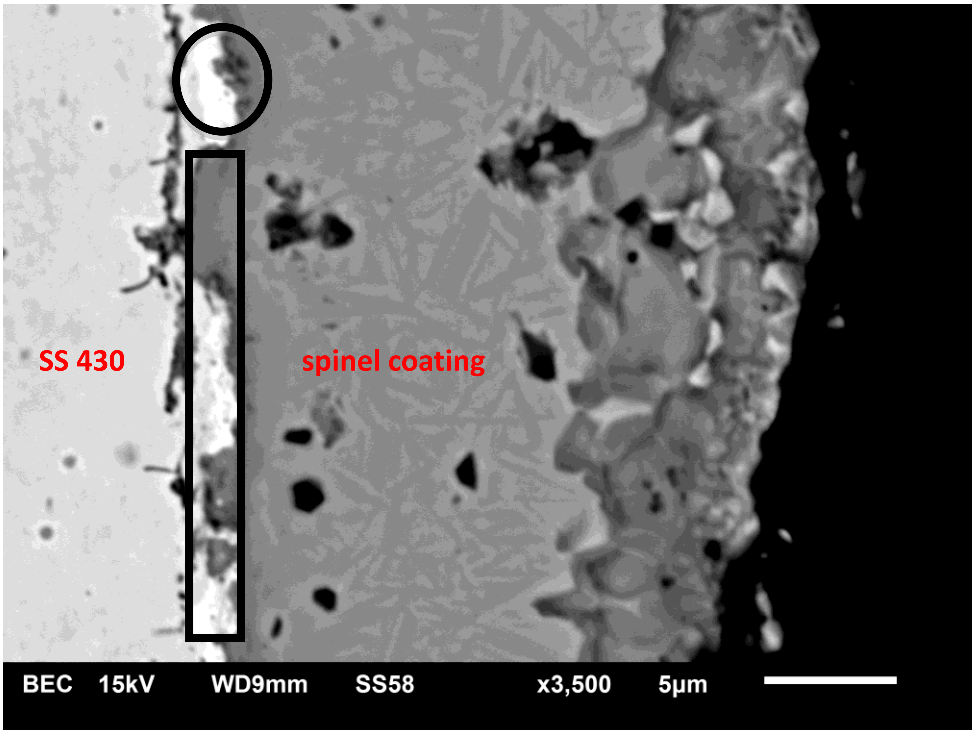

Figure 5.10 $Co_{0.5}Cu_{0.5}Mn_2O_4$ coating on stainless steel oxidized for 24 h

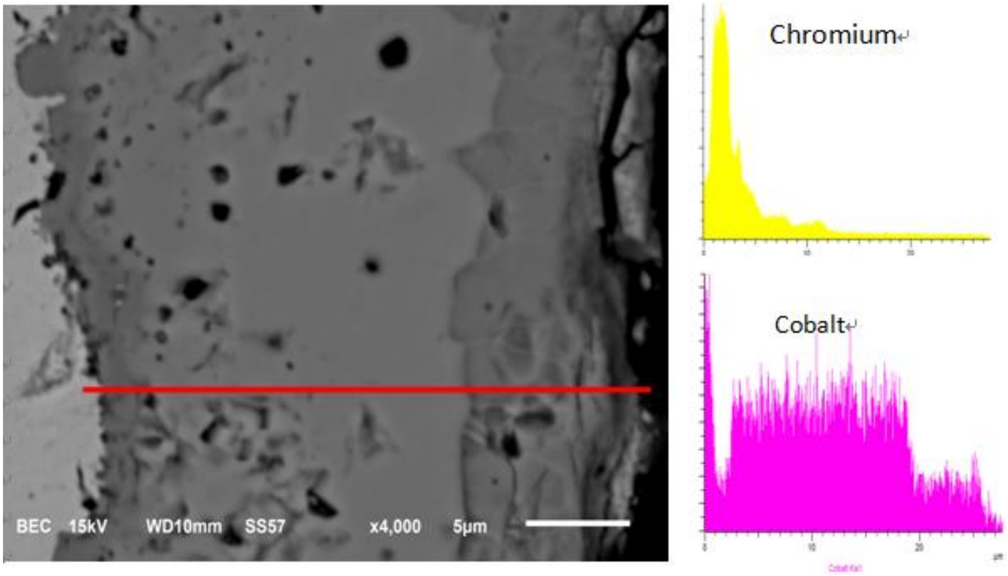

Figure 5.11 $Co_{0.5}Cu_{0.5}Mn_2O_4$ coating on stainless steel oxidized for 120 h, SEM photo (left) and EDS measurements for chromium and cobalt.

Figure 5.11 shows the result after 120 hours oxidation of the same coating. The spinel coating layer is about 25 microns in thickness and appears as two phases. EDS results indicate that the outer layer is rich in manganese and oxygen with minor amounts of cobalt and copper. This phenomenon could be due to excess manganese deposition, resulting in manganese oxide outside the spinel coating. A thin layer, which is about 3 μm, lying between the coating and substrate is the chromia scale which is easily visible here compared with the 24 hour oxidation sample. The coating has some pores present, especially along the chromia layer. Since chromium is more easily oxidized than cobalt, metallic chromium in the solid solution diffuses to the substrate surface and forms oxide, leaving cobalt behind. Compared with 24 hours oxidation, the trapped metallic cobalt from the solid solution diffuses into the stainless steel substrate.

5.3.1.2 On Chromium Alloy Substrate

Figure 5.12 is the SEM photo of $Co_{0.5}Cu_{0.5}Mn_2O_4$ coating on the Cr-5Fe plate after 24-hour oxidation. The chromia scale forms a thick layer due to high chromium content. Behind the chromia, there is a very bright, thin phase identified by EDS as metallic copper. A layer of cobalt-chromium solid solution, almost 3 μm thick is found beneath the metallic copper phase. Between the solid solution phase and substrate, a 2 μm thick porous nitride is observed. This crystalline nitride material could cause poor adhesion of the coating.

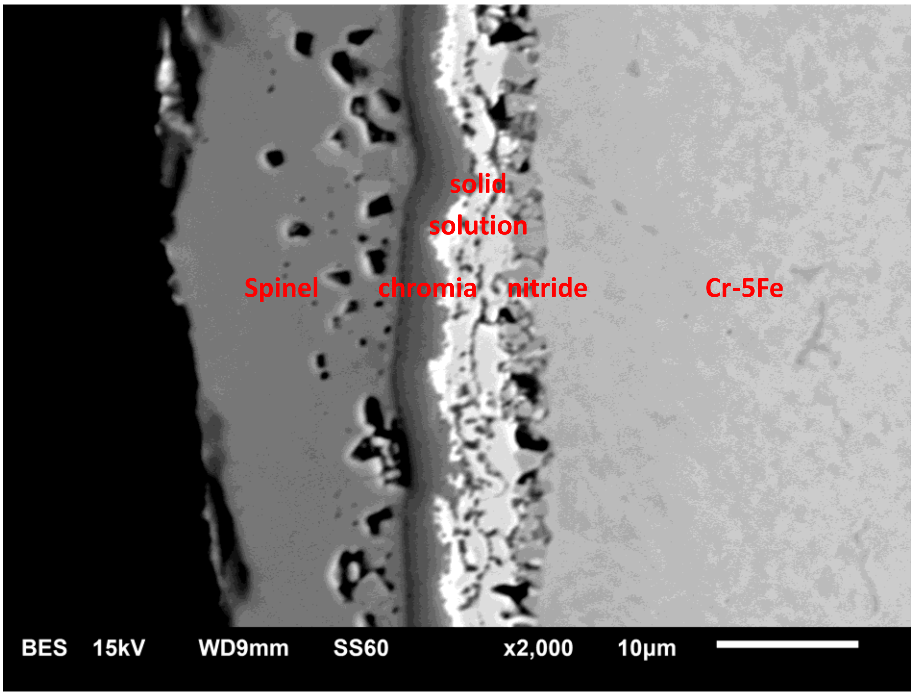

Figure 5.12 $Co_{0.5}Cu_{0.5}Mn_2O_4$ spinel coating on Cr-5Fe, oxidized for 24h in air

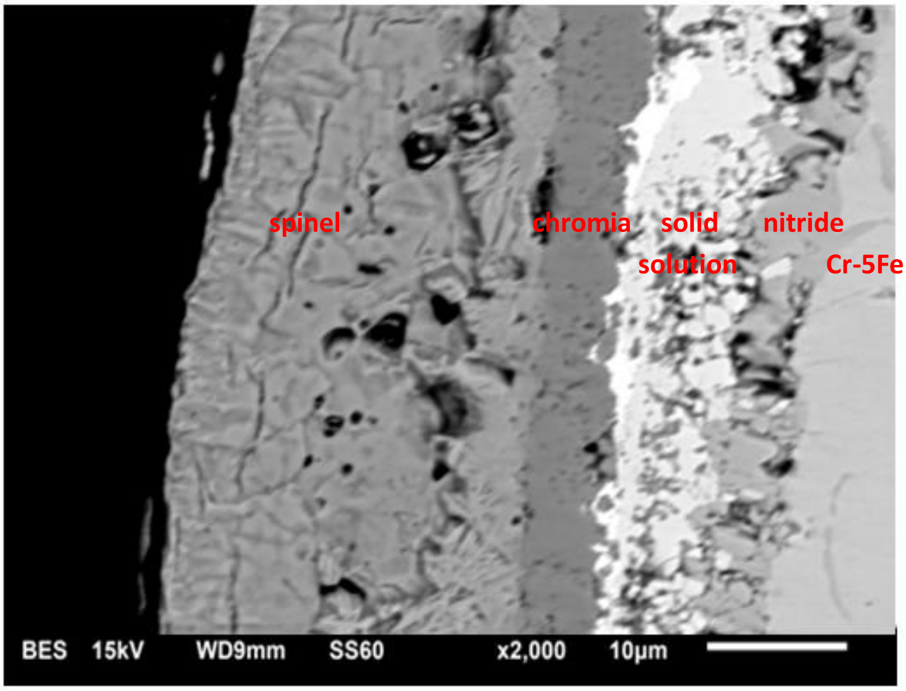

Figure 5.13 $Co_{0.5}Cu_{0.5}Mn_2O_4$ spinel coating on Cr-5Fe, oxidized for 120 h in air

Figure 5.13 is the SEM micrograph of $Co_{0.5}Cu_{0.5}Mn_2O_4$ coated Cr-5Fe plate after 120-hour oxidation. Compared with 24 hour oxidation results, the coating is more dense with fewer pores. The chromium oxide scale increases to about 6 μm while the chromium-cobalt solid solution remains unchanged. The composition of the spinel coating deviated from the targeted composition as approximately $Co_{0.3}Cu_{0.4}Mn_{2.3}O_4$. In addition, the nitrides become more fragmentary.

Comparing the coating features on the two different substrates, two differences can be noted:

- The first is that the coating is more porous in the region beside chromia on chromium plate than on stainless steel. This could be due to the oxidation mechanism of chromium. For alloys, when the content of chromium is below 10%, it prefers to form spinel on the surface while when the content is above 20%, the chromium will form sesquioxide. Stainless steel, whose chromium content is 16~18%, will form an chromium oxide layer and a very thin Cr-Mn-O spinel layer which will later dissolve into or be covered by spinel coating (Bateni et al, 2007) leading to good adhesion between chromia and the coating, while for Cr-5Fe plate, only chromia scale is formed on the surface and the adhesion between substrate and coating may be relatively poor.

- The second is the nitride problem, which is common on Cr-5Fe plate while hardly observed on stainless steel. It also tends to promote detachment of the spinel coating.

5.3.1.3 $Co_{0.5}CuMn_{1.5}O_4$ Spinel on Chromium Alloy Substrate

Another composition of $Co_{0.5}CuMn_{1.5}O_4$ was applied on chromium plate using the same deposition and heat treatment parameters. Figure 5.14 shows a $Co_{0.5}CuMn_{1.5}O_4$ coating oxidized in air for 120 hours. The character is very similar to that in Figure 5.13. The chromia scale is approximately 6 μm in thickness. Behind the chromia, there is a layer of Co-Cr solid solution with a small copper content. The nitride layer between the substrate and solid solution is discontinuous and porous, with a high probability of poor adhesion.

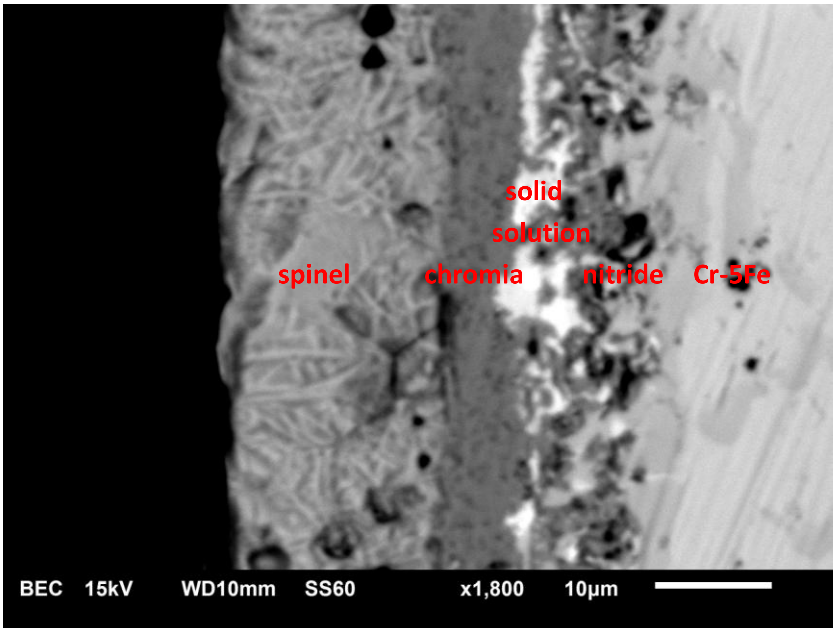

Figure 5.14 $Co_{0.5}CuMn_{1.5}O_4$ spinel coating on Cr-5Fe, oxidized for 120h in air

Based on these experiments, several problems can be noted.

- The first is the nitride which usually exists between chromia and the substrate on chromium alloy. Iron and chromium can both form nitrides. But at high temperatures, iron nitrides are not stable and will decompose. Chromium nitride is a chemical compound with the formula Cr_2N. It is very hard, also extremely resistant to corrosion. In addition, chromium nitride is an interstitial compound, whose nitrogen atoms occupy octahedral holes in the chromium lattice. Chromium also forms a second interstitial nitride, CrN, which has even lower conductivity. Chromium nitride is responsible for poor adhesion of the coating to the substrate and should be eliminated.
- The second problem is blistering of the outer layer of coating, as is shown in Figure 5.15.

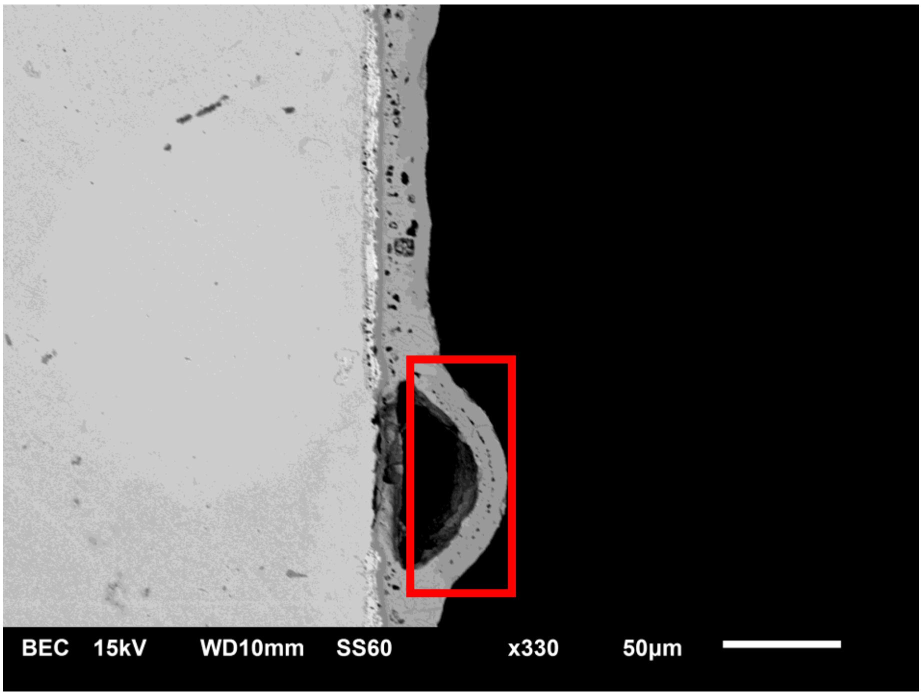

Figure 5.15 Problem of "blistering" of coating

The diameter of the blister is as large as 80 μm. EDS measurement shows that the bubbled shell is mainly manganese oxide. It could be formed at the beginning of oxidation process since manganese is far more easily oxidized than cobalt and copper. The mismatch due to thermal expansion may lead to the "blistering" phenomenon.

- The third problem is that the isolated metal (cobalt and copper) will not be incorporated into the spinel coating which will lead to a change in coating composition and a waste of material. Since chromium has a high oxidation affinity, it tends to diffuse outward immediately in an oxygen environment. Thus a spinel coating needs to form as soon as possible to block chromium diffusion and oxidation.

A schematic diagram can be constructed for better understanding of the problems. At the beginning of the oxidation process, the out layer of manganese is oxidized because of strong oxidation affinity, metals begin to diffuse and a solid solution of chromium with cobalt is formed, shown as Figure 5.16. As oxidation proceeds, the air diffuses into the substrate surface and chromium diffuses out, leading to the formation of chromia scale and nitride. Spinel coating is also gradually formed at the same time, shown as Figure 5.17.

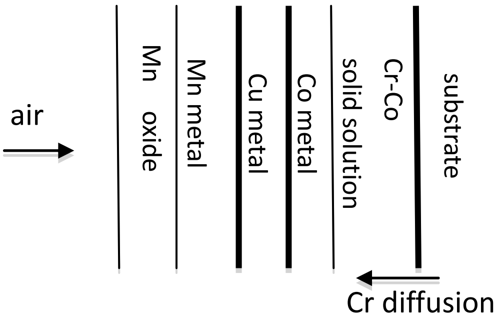

Figure 5.16 Start of diffusion and oxidation process

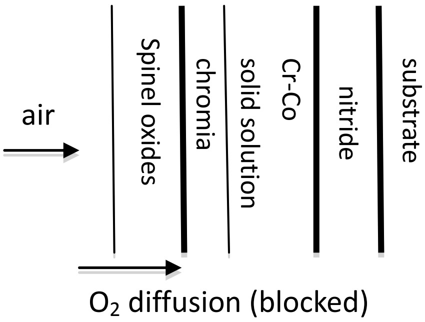

Figure 5.17 Steady state of diffusion and oxidation process

Based on these problems, the heat treatment parameters were modified to optimize the spinel coating.

5.3.2 Oxidation in Pure Oxygen

Since the source of the nitrides is nitrogen in air, pure oxygen was applied to eliminate the source of nitrogen. The chromium plate with $Co_{0.5}Cu_{0.5}Mn_2O_4$ spinel coating was oxidized in pure oxygen at 800^{o}C for 120 hours.

The oxidized coating was shiny and dark grey in color, very different from the air oxidized sample (golden in color). Also, this coating is very fragile and easily falls off during cutting. This could be due to too high oxidation rate of the coating layer resulting in mismatch with substrate due to the difference in thermal expansion coefficient. Figure 5.18 shows an SEM image of the residual coating. The spinel is very porous and has a large amount of dentritic phase. Compared with Figure 5.13, the chromia scale labeled 2 in the micrograph is thicker (about 10 µm). Beneath the chromia, there is a layer, labeled 3, rich in cobalt, iron and chromium based on EDS analysis. The layer labeled 4 also has an unusual composition of chromium, copper and oxygen, which means the chromium in the alloy is diffusing out, leaving copper trapped inside. Although the pure oxygen heat treatment successfully eliminated the nitrides, it is not an effective way to convert the coating to spinel due to the following reasons:

1) Thicker chromia scale formed.
2) More oxygen penetrated through coating and oxidized the substrate.
3) More iron diffused out to the spinel scale.
4) More trapped cobalt and copper between chromia and substrate.
5) Poor attachment.

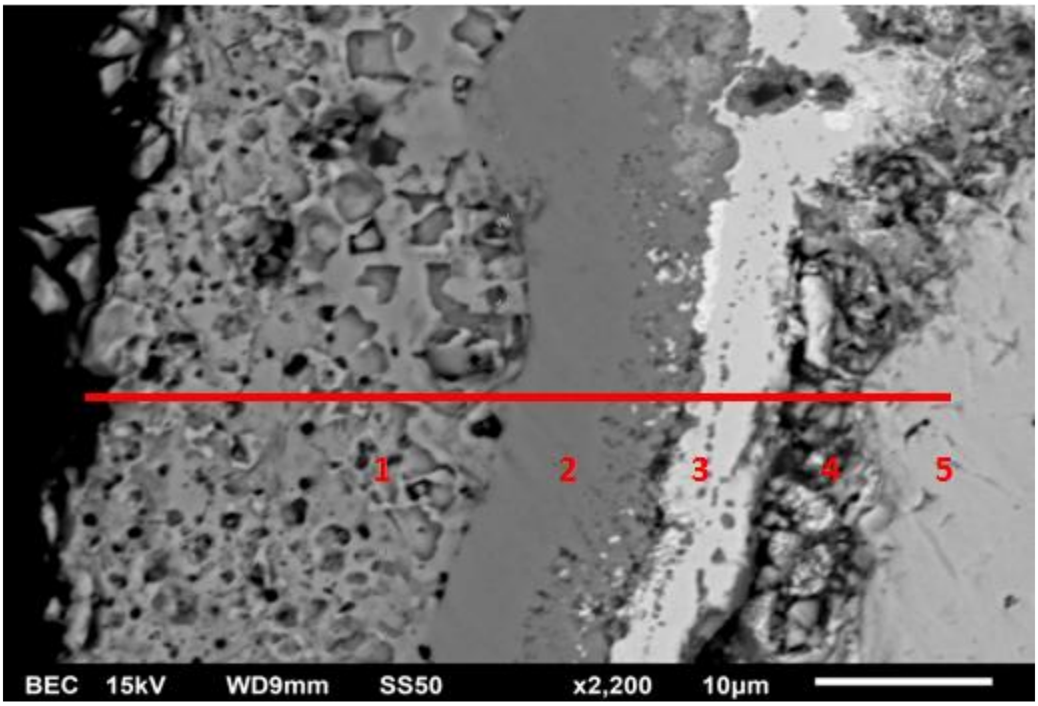

Figure 5.18 $Co_{0.5}Cu_{0.5}Mn_2O_4$ spinel coating on Cr-5Fe, oxidized for 120 h in pure oxygen

Since excessive oxidation rate can cause serious damage to the coating, two possible methods were tried to reduce this problem.

1. The first was pre-heating in hydrogen. This should help mix the metals together to become homogenous. After annealing in H_2, oxidation should quickly produce spinel coatings and therefore slow down the oxygen penetration rate to the substrate.
2. The other way could be by decreasing the oxygen partial pressure, thus decreasing the oxidation rate.

The $Co_{0.5}Cu_{0.5}Mn_2O_4$ spinel was coated on chromium plate, annealed in hydrogen for 24 hours at 800°C and oxidized in pure oxygen for 96 hours. The result shows that pre-heating in hydrogen cannot successfully solve the problem of rapid oxidation, but it improves the metal mixing and coating adhesion compared to the coating in Figure 5.16.

From the low magnification SEM photo (Figure 5.19), it is observed that the coating layer is porous and not uniform, especially the outermost part. There is a layer of trapped metal next to the substrate, seen as the white phase in the photo.

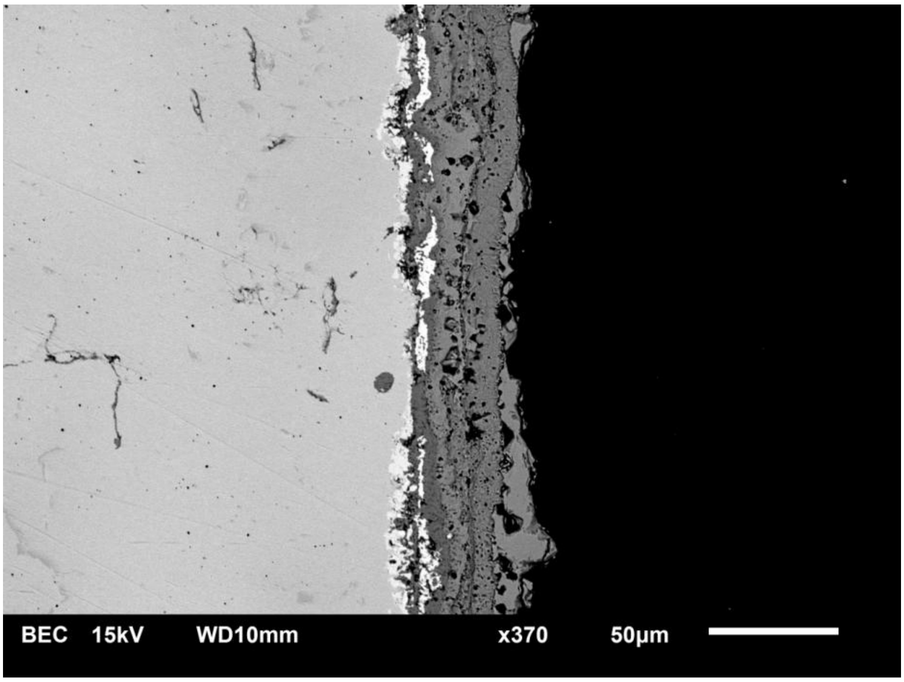

Figure 5.19 Low magnification of $Co_{0.5}Cu_{0.5}Mn_2O_4$ coating on Cr-5Fe, annealed in hydrogen for 24 h 800°C followed by oxidation in pure oxygen for 96 h at 800°C

EDS analysis at high magnification revealed the white trapped metal is a solid solution of cobalt mixed with chromium and a trace amount of iron. In front of the solid solution is the chromia scale which is about 7 μm in thickness. The coating appears to have two phases. One is a Cu-Mn-O spinel phase and the outer one is manganese oxide with embedded copper based on EDS analysis.

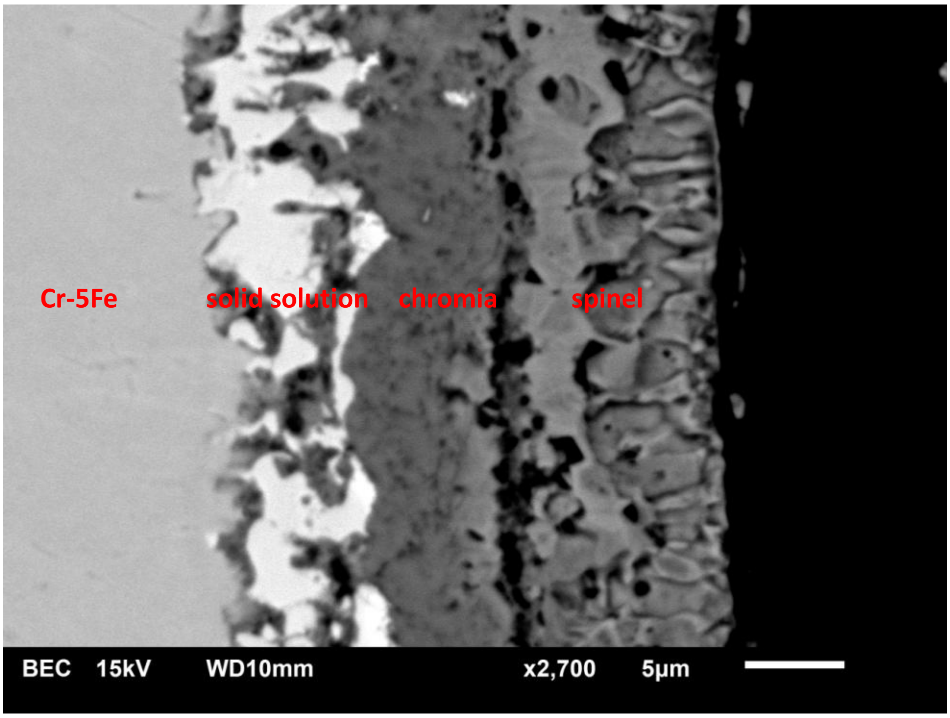

Figure 5.20 High magnification of $Co_{0.5}Cu_{0.5}Mn_2O_4$ coating on Cr-5Fe, annealed in hydrogen for 24 h 800°C followed by oxidation in pure oxygen for 96 h at 800°C

5.3.3 Effect of Oxygen Concentration during Oxidation

5.3.3.1 Oxidation in Humidified Argon

$Co_{0.5}Cu_{0.5}Mn_2O_4$ spinel was coated on chromium plate, annealed in hydrogen for 24 hours at 800°C and oxidized in humidified argon for 72 hours at 800°C. This experiment was aimed at lowering the oxygen concentration in order to lower the oxidation rate. The SEM photo (Figure 5.21) showed chromia layer did not form on top of the Co-Cu metallic layer. The layer on left is the coating that is about 10 μm, and between the coating and the substrate, there is a 7 μm thick metallic layer, seen as white in the photo.

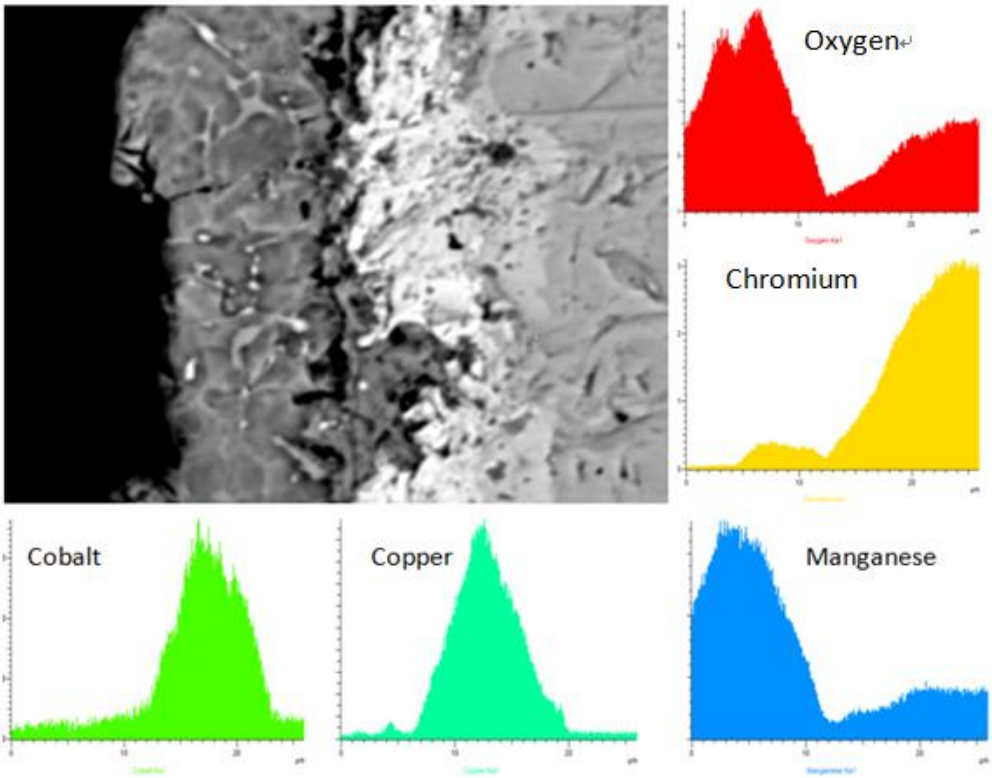

Figure 5.21 SEM photo and EDS result of $Co_{0.5}Cu_{0.5}Mn_2O_4$ coating on Cr-5Fe, annealed in hydrogen and oxidized in humidified argon

EDS linescan results of oxygen, chromium, cobalt, copper and manganese were demonstrated in Figure 5.21. Chromium is almost stopped at the interface and has a small amount diffused into the coating layer. The coating contains mainly manganese mixed with some copper. Copper is partly mixed with cobalt and cobalt is mainly dissolved into the chromium.

The EDS results indicate that manganese is totally oxidized while Co-Cr solid solution is partly oxidized but not forming chromia due to the low oxygen content. However the copper still remains in the metallic state meaning the oxygen partial pressure is not high enough to oxidize copper.

This can be explained by the following calculation. The humidified argon, formed by bubbling Ar through water, contains saturated H_2O vapor partial pressure of 3%. We can use the equation $H_2 + 0.5\ O_2 = H_2O$ to calculate the equilibrum oxygen partial pressure at $800^{o}C$.

$\Delta G = -247500+55.85T = -187572.95\ (J) = -RT\ln(K) = -RT\ln(\frac{P_{H_2O}}{P_{H_2} * P_{O_2}^{1/2}})$

By solving this equation, the value of oxygen partial pressure is found as

$P_{O_2} = 4 * 10^{-10}$ atm (if total pressure is regarded as 1 atm)

For copper, $Cu + 0.5\ O_2 = Cu_2O$, the partial pressure of oxygen that is required for oxidation can be calculated as:

$\Delta G = -162200 + 69.24T = -87905.48\ (J) = -RT\ln(K) = RT\ln\ (P_{O_2})$

$P_{O_2} = 3.1 * 10^{-9}$ atm

The given partial pressure of oxygen is lower than the minimum required pressure, and thus the copper cannot be oxidized.

During hydrogen annealing at $800^{o}C$, cobalt and chromium can form a solid solution due to high solubility. This can trap the metallic cobalt at the interface. On the other hand, copper and chromium are totally insoluble.

From this aspect, depositing copper first should improve the composition of the coating, but in order to improve the attachment, 30 second of cobalt deposition was used before electroplating copper.

5.3.3.2 Oxidation in 1% O_2

$Co_{0.5}Cu_{0.5}Mn_2O_4$ spinel was coated on chromium plate, annealed in hydrogen for 24 hours at 800°C and oxidized in 1% O_2 with 99% Ar at 800°C.

In this experiment, 1% O_2, referring to 10^{-2} atm, should be high enough to oxidize all the metals.

Figure 5.22 is the SEM image at high magnification. Copper was deposited as the first layer in order to reduce trapped metal during annealing. The spinel coating is uniform without delamination. Between the spinel coating and the chromium oxide, a porous band still exists. Beneath the chromia scale, there is a Co-Cr solid solution with copper as a minor phase, shown as white phase in the photo. The chromia scale is approximately 4 µm thick. One unusual spot in the image is the region in the box. This area is rich in chromium, cobalt and oxygen. This kind of isolated oxide has only been observed in the pure oxygen oxidation experiment. A possible explanation is that some defects on the substrate promoted rapid chromium outward diffusion, or the defect in the spinel coating produced during deposition resulted in fast oxygen penetration.

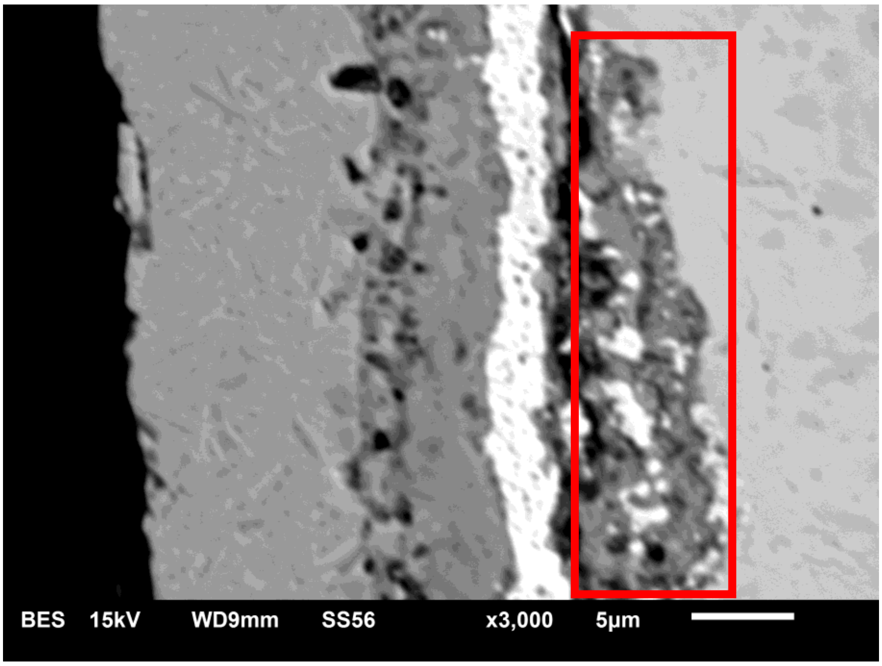

Figure 5.22 $Co_{0.5}Cu_{0.5}Mn_2O_4$ coating on Cr-5Fe, annealed in hydrogen and oxidized in 1% O_2 with 99% Ar

Generally speaking, the quality of the coating has been improved significantly as it is more uniform with less blistering, and the amount of trapped cobalt is decreased.

5.3.4 Effect of Hydrogen Annealing

One may argue that the low oxygen partial pressure oxidation without annealing may be enough to reduce the blistering phenomenon. In order to understand the effect of hydrogen annealing, an experiment of oxidizing in 1% oxygen and 99% argon for 24 hours was carried out and the coating cross-section was shown in Figure 5.23. It is obvious to see that although the oxidation rate was very slow, blistering still occurred, which also indicates that annealing in hydrogen is needed to eliminate blisters.

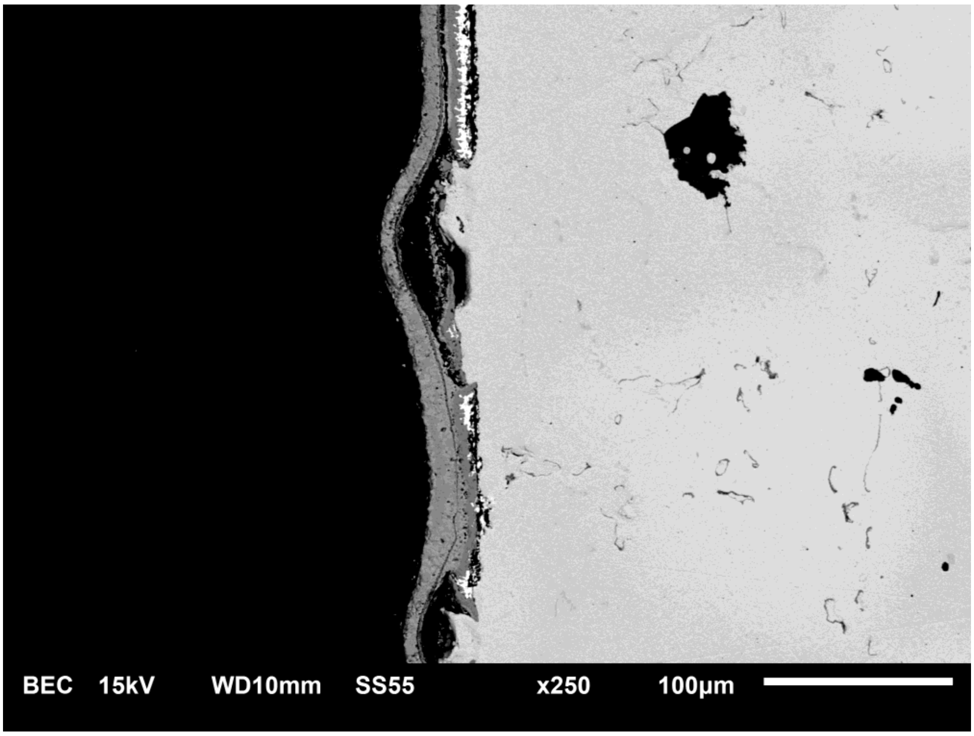

Figure 5.23 1% oxygen and 99% argon oxidizing result

Effect of Increased Hydrogen Annealing Temperature

In an effort to improve the metal mixing so as to decrease the time needed to form the spinel phase, the hydrogen annealing temperature was increased to 950°C. Figure 5.24 shows the result of $Co_{0.5}Cu_{0.5}Mn_2O_4$ coating on chromium plate annealed in hydrogen at 950°C and then oxidized in oxygen in 1% oxygen for 24 hours. By visual inspection, the coating is very well attached, uniform and dense. However EDS analysis shows that the area in the box is a chromium-cobalt solid solution. On top of the Cr-Co solid solution is a band of copper metal, which appears as a bright white phase in the image. A thin layer of chromia located next to the copper phase. In fact, almost all cobalt and copper are trapped behind the chromia, leaving just a little dissolved into the coating, which means the coating is essentially only manganese oxide.

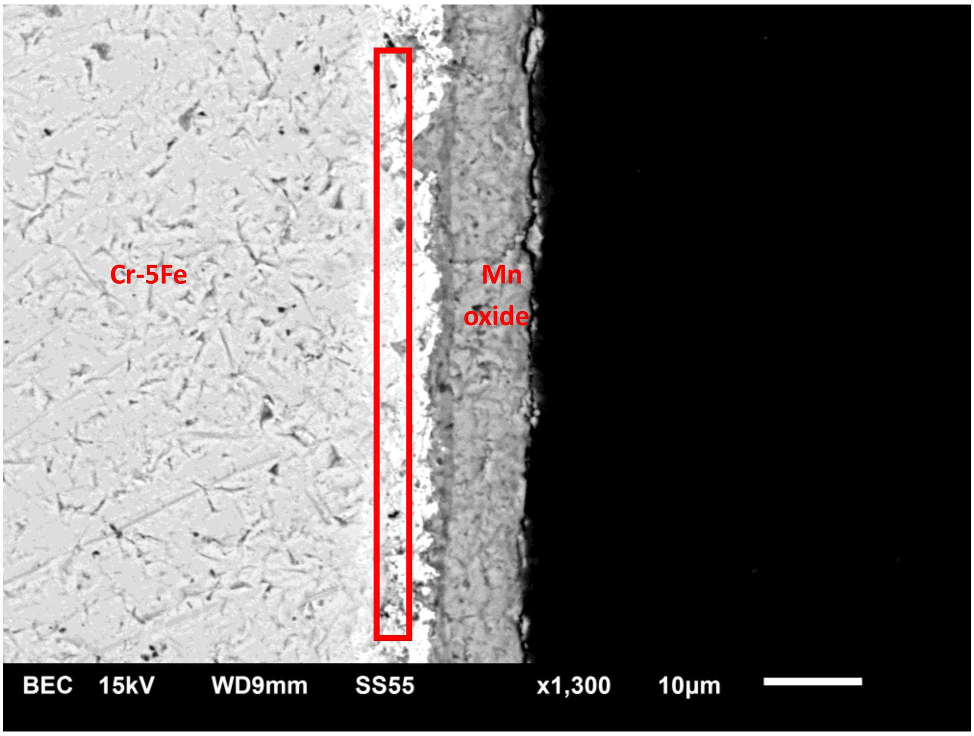

Figure 5.24 Temperature of 950°C hydrogen annealing result

This image gives an extreme example with all cobalt and copper being trapped while in other areas, copper is usually 50% trapped. Therefore it is apparent that although copper and chromium don't form a solid solution, metals still can transfer through each other. High annealing temperature greatly increases the diffusion rate. Copper has much better mobility than cobalt since copper diffused into both the substrate and the coating.

5.3.5 Effect of Lower Oxidation Temperature

The $Co_{0.5}Cu_{0.5}Mn_2O_4$ spinel was coated on chromium plate, annealed in hydrogen for 24 hours at 800°C and oxidized in 1% O_2 with 99% Ar at 600°C for 10 hours and then 800°C for 24 hours. The coating appears good at low magnification, as is shown in Figure 5.25. There is absolutely no blistering evident and the coating is uniform as well as flat. In addition the chromia scale is thinner compared with previous experiments. Chromium has much lower diffusion rate at 600°C while spinel can still form at this temperature. Once a spinel layer about 1 μm is formed on top, the oxidation kinetics of chromium will slow down changing from parabolic to linear (Virkar et al, 2005). Thus the thickness of chromia will decrease. Still the problem of trapped metal exists, with both copper and cobalt, shown by the boxed area in the image.

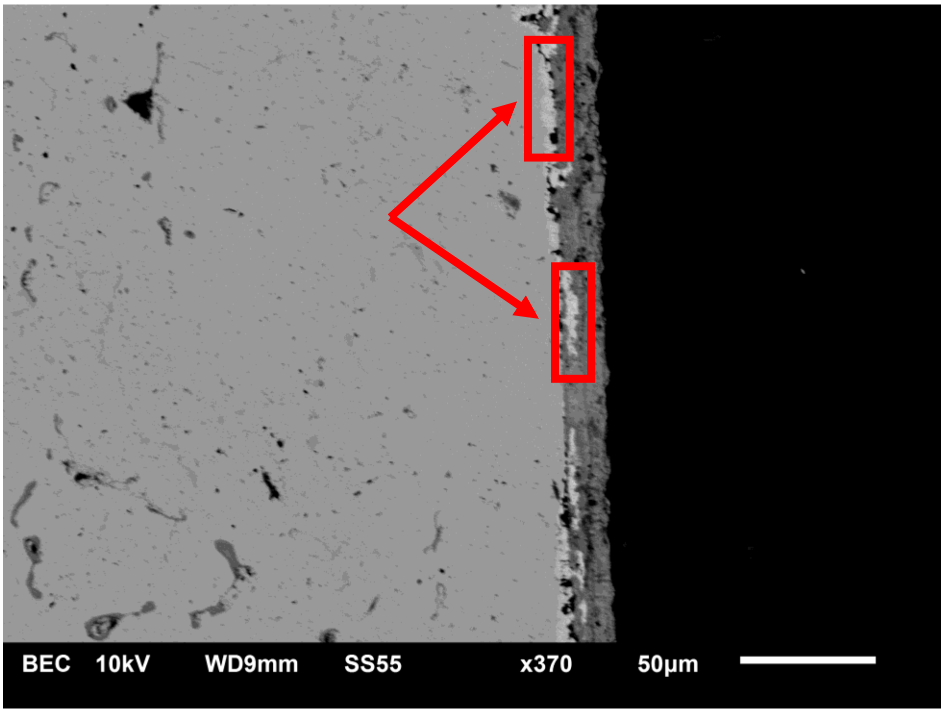

Figure 5.25 $Co_{0.5}Cu_{0.5}Mn_2O_4$ coating on Cr-5Fe, annealed in hydrogen and oxidized in 1% O_2 with 99% Ar at 600°C for 10 h and then 800°C for 24 h

5.3.6 Coating at the Edge

As mentioned before, the coating is sometimes thicker at the edge than in the center due to the deposition process. Actually, these regions show better coating quality.

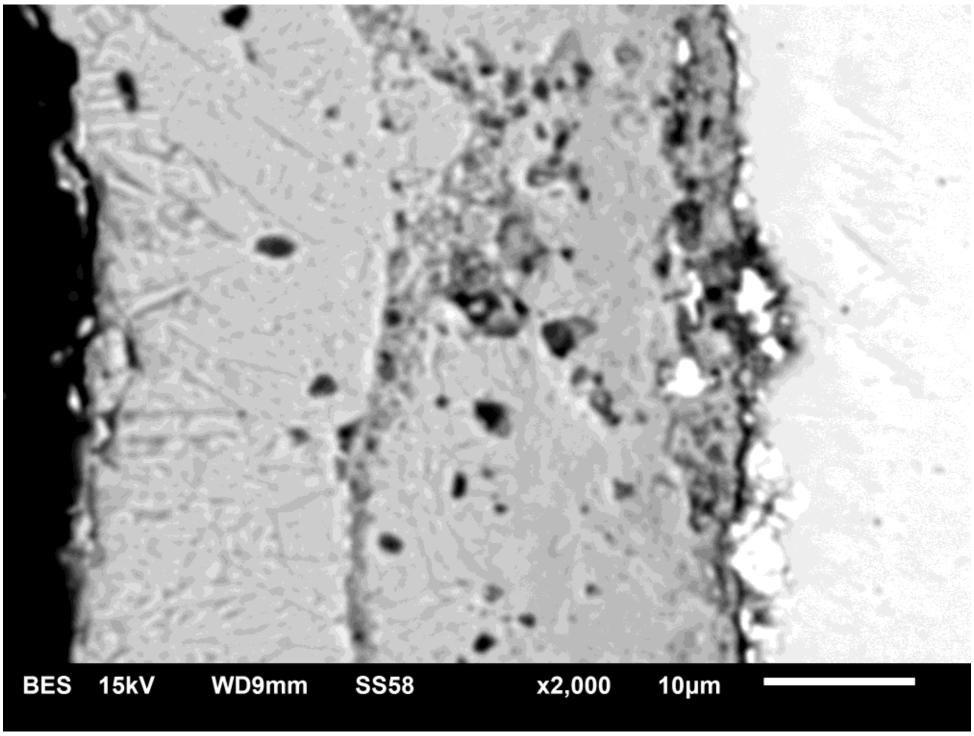

Figure 5.26 Coating at the edge

Figure 5.26 is the image from the edge of one sample annealed in hydrogen for 24 hours and then oxidized in 1% oxygen for 24 hours. The coating is approximately 40 μm in thickness, more than twice as thick as expected. It is uniform with some small pores remaining. The chromia is about 4 μm thick and between the chromia and coating is a layer of chromium containing spinel. Only a fraction of copper and cobalt was trapped between the chromia scale and the substrate. These indicate that the coating is a very efficient protective layer. However when the thickness of coating is doubled from the deposition process, all the advantages disappear due to other problems.

Chapter 6

Summary and Conclusion

In this work, two groups of spinels were investigated, Zn-Mn-O system and Co-Cu-Mn-O system.

The Zn-Mn-O spinel has low electrical conductivity at SOFC generating temperatures (800^{o}C), since it presents deformed tetragonal spinel phase at low zinc content and a two-phase region composed of spinel and zinc oxide at high zinc content based on in situ high temperature XRD results. Pure cubic phase only exists in a narrow range at high temperatures (above 1200^{o}C); thus this kind of spinel is not acceptable for the interconnect coating.

In contrast, Co-Cu-Mn-O spinels have higher electrical conductivity over a wide composition range. $Co_{0.5}Cu_{0.5}Mn_2O_4$ was chosen as the optimum composition for the spinel coating because of its good conductivity values as well as decreased cost of cobalt.

Two types of substrates, 430 stainless steel (16% ~ 18% chromium) and chromium alloy (95% chromium + 5% iron) were used to test the quality of coatings. Metals were electodeposited onto the substrate and then oxidized to form a spinel structure. Ambient air oxidation was first performed for 24 and 120 hours at 800^{o}C on the two kinds of substrates. Spinel on stainless steel was quickly formed with a thin layer of Cr_2O_3 scale between the coating and the substrate. The oxidation process was slow on chromium plate and many problems were encountered: a layer of nitrides formed between the substrate and the chromia scale gave poor adhesion; metallic copper and cobalt were isolated beneath the chromia, affecting the composition of the coating and blistering phenomenon made the coating discontinuous and nonuniform. Thus heat treatment parameters were adjusted to optimize the coating quality. With hydrogen annealing prior to oxidation, metals were uniformly mixed and thus eliminated the blisters; with low oxygen concentration in the oxidation atmosphere (1% O_2 + 99% Ar), the coating was dense without nitrides formed; with low oxidation temperature, the chromium diffused slowly while spinel coating still could form and thus reduce the thickness of chromia.

However, no proper method was found to eliminate the metal isolation problem and further research is needed.

Bibliography

Arillo, M. A., Lopez, M. L., Perez-Cappe, E., Pico, C. & Veiga, M. L. (1998). Crystal Structure and Electrical Properties of $LiFeTiO_4$ Spinel. *Solid State Ionics, 107,* 307-312

Aruna, S. T., Muthuraman, M. & Patil, K. C. (1997). Combustion Synthesis and Properties of Strontium Lanthanum Manganites $La_{1-x}Sr_xMnO_3$ ($0 \le x \le 0.3$). *Journal of Materials Chemistry, 7(12)*, 2499-2503

Bateni, M. R. (2012). *http://www.mie.utoronto.ca/labs/sofc/reza_bateni.html*

Bateni, M. R., Wei, P., Deng, X. & Petric, A. (2007). Spinel Coatings for UNS 430 Stainless Steel Interconnects. *Surface & Coating Technology, 201*, 4677-4684

Blasco, J. & Garcia, J. (2006). Stable Cubic Spinels in the Zn-Mn-O System in Air. *Journal of Solid State Chemistry, 179,* 2199-2205

Craig Fisher (2013). *http://people.bath.ac.uk/cf233/sofc.html*

Chen, X., Hou, P. Y., Jocaob C. P., Visco, S. J. & De Jonghe, L. C. (2005). Protective Coating on Stainless Steel Interconnect for SOFCS: Oxidation Kinetics and Electrical Properties. *Solid State Ionics 176,* 425-433

De Souza, S., Visco, S. J. & De Jonghe, L. C. (1997). Reduced-Temperature solid oxide fuel cell based on YSZ thin-film electrolyte. *Journal of the Electrochemical Society, 144*, L35

De Souza, S., Visco, S. J. & De Jonghe, L. C. (1997). Thin-film solid oxide fuel cell with high performance at low temperature. *Solid State Ionics, 98*, 57

Deng, X., Wei, P., Bateni, M. R. & Petric, A. (2006). Cobalt Plating of High Temperature Stainless Steel Interconnects. *Journal of Power Sources, 160,* 1225-1229

Dorris, S. E. & Mason, T. O. (1988). Electrical Properties and Cation Valencies in Mn_3O_4. *Journal of the American Ceramic Society, 71 (5),* 379-85

Fergus, J. W. (2004). Lanthanum chromite-based Materials for Solid Oxide Fuel Cell Interconnects. *Solid State Ionics 171,* 1-15

Huang, K., Hou, P. Y. & Goodenough, J. B. (2000). Characterization of Iron-based Alloy Interconnects for Reduced Temperature Solid Oxide Fuel Cells. *Solid State Ionics 129*, 237-250

Horita, T., Xiong, Y., Kishimoto, H., Yamaji, K., Sakai, K., Brito, M. E. & Yokakawa, H. (2001). Oxide Scale Formation on Alloy Interconnect in CH_4 Fuels for Solid Oxide Fuel Cells. *Solid Oxide Fuel Cells IX, PV 2005-07*, 1822-31
Irvine, J. T. S. & Connor, P. (2013). *Soild Oxide Fuel Cells: Facts and Figures*

Joffe, A.(1960). *Physics of Semiconductors. Infosearch Ltd., London.*

Khurmi, R. S., *Material Science.*

Lowenheim, F. A. (1978). *Electroplating*. USA: McGraw-Hill

Montero, X., Jordan, N., Piron-Abellan, J., Tietz, F., Stover, D. & Cassir, M. (2009). Spinel and Perovskite Protection Layers Between Crofer 22APU and $La_{0.8}Sr_{0.2}FeO_3$ Cathode Materials for SOFC. *Journal of the Electrochemical Society 156(1)*, B188-B196

Nice, K. & Strickland, J., *How Fuel Cells Work: Polymer Exchange Membrane Fuel Cells How Stuff Works.*

Ostwald, C. & Grabke, H. J.(2004). Initial Oxidation and Chromium Diffusion. I. Effects of Surface Working on 9-20% Cr Steels. *Corrosion Science, 46,* 1113-1127

Paulsen, J. M. & Dahn, J. R. (1999). Phase Diagram of Li-Mn-O Spinel in Air. *Chemistry of Materials, 11,* 3065-3079

Petric, A. & Ling, H. (2006). Electrical Conductivity and Thermal Expansion of Spinels at Elevated Temperatures. *Journal of the American Ceramic Society, 90(5),* 1515-1520

Peiteado, M., Sturm, S., Caballero, A. C. & Makovec, D. (2008). $Mn_{3-x}Zn_xO_4$ Spinel Phases in the Zn-Mn-O System. *Acta Materialia, 56,* 4028-4035

Qu, W., Jian, L., Hill, J. M. & Ivey, D. G. (2006). Electrical and Microstructure Characterization of Spinel Phases as Potential Coatings for SOFC Metallic Interconnects. *Journal of Power Sources, 153*, 114-124

Quadakkers, W. J., Piron-Abellan, J., Shemet, V. & Singheiser, L. (2003).

Metallic Interconnects for Solid Oxide Fuel Cells-A Riview. *Materials at High Temperatures 20(2),* 115-127

Singhal, S.C. & Kendall, K., *High Temperature Solid Oxide Fuel Cells: Fundamentals, Design and Applications*

Shaigan, N., Ivey, D. G. & Chen, W. (2008). Co/$LaCrO_3$ Composite Coatings for AISI 430 Stainless Steel Solid Oxide Fuel Cell Interconnects. *Journal of Power Sources, 185*, 331-337

Shaigan, N., Ivey, D. G. & Chen, W. (2008). Oxidation and Electrical of Nickle/Lanthanum Chromite-coated Stainless Steel Interconnects. *Journal of Power Sources, 183,* 651-659

Shaigan, N., Qu, W., Ivey, D. G. & Chen, W. (2010). A Review of Pecent Progress in Coatings, Surface Modifications and Alloy Developments for Solid Oxide Fuel Cell Ferritic Stainless Steel Interconnects. *Journal of Power Sources, 195,* 1529-1942

Sylla, D., Savall, C., Gadouleau, M., Rebere, C., Creus, J. & Refait, Ph. (2005). Electrodeposition of Zn-Mn Alloys on Steel Using Alkaline Pyrophosphate-based Electrolytic Bath. *Surface and Coatings Technology, 2000 (7)*, 2137-2145

Toussaint, H. (1964). Solid State Reactions of MnO_2 and Mn_2O_3 with CaO, ZnO, MgO, and CdO. *Revue De Chimie Minérale, 1(2),* 141-95

Wand, G., *Fuel Cells History (part 1).*

Wei, F., Chen, W. & Ivey, D. G. (2007). Anodic Electrodeposition of Nanocrystalline Coatings in the Mn-Co-O System. *Chemistry of Materials, 19*, 2816-1822

Wei, F., Chen, W. & Ivey, D. G. (2009). Oxidation Resistance and Electrical Properties of Anodic Electrodeposited Mn-Co Oxide Coatings for Solid Oxide Fuel Cell Interconnect Applications. *Journal of Power Sources, 186*, 428-434

Wu, J., Johnson, C. D. & Liu, X. (2008). DC Electrodeposition of Mn-Co Alloys on Stainles Steels for SOFC Interconnect Application. *Journal of Power Sources 177,* 376-385

Wu, J., Johnson, C. D., Gemmen, R. S. & Liu, X. (2009). The Performance of

Solid Oxide Fuel Cells with Mn-Co Electroplated Interconnect as Cathode Current Collector. *Journal of Power Sources, 189,* 1106-1113

Yang, Z., Xia, G., Simner, S. P. & Stevenson, J. W. (2005). Thermal Growth and Performance of Manganese Cobaltite Spinel Protection Layers on Ferritic Stainless Steel SOFC Interconnects. *Journal of the Electrochemistry Society, 152(9),* A1896-A1901

Zhu, W. Z. & Deevi, S. C. (2003). Development of Interconnect Materials for Solid Oxide Fuel Cells. *Materials Science & Engineering A, 348,* 227-243

Appendix A Conductivity Test Results

Conductivity test results of Zn-Mn-O system

Temperature(°C)	0.1 σ (S/cm)		0.4 σ (S/cm)		0.6 σ (S/cm)	
	Cooling	heating	cooling	heating	cooling	heating
600	0.005589	0.005631	0.007124	0.006921	0.00755	0.00712
700	0.023403	0.024633	0.030339	0.030981	0.047884	0.047041
800	0.083375	0.089666	0.106053	0.11086	0.171412	0.163875
900	0.276288	0.308591	0.372382	0.353625	0.546715	0.527621
Temperature(°C)	**1.0 σ (S/cm)**		**1.2 σ (S/cm)**		**1.4 σ (S/cm)**	
	Cooling	heating	cooling	heating	cooling	heating
600	0.015475	0.014638	0.590066	0.574229	0.6321	0.606452
700	0.072449	0.06591	1.131975	1.088042	1.272268	1.224567
800	0.21294	0.217256	2.110458	2.087994	2.59061	2.496848
900	0.57642	0.569597	4.100873	4.019453	4.923954	4.760294

Conductivity test results of Co-Cu-Mn-O system

Temperature(^{o}C)	**$CoMn_2O_4$ σ (S/cm)**		**$Co_{0.8}Cu_{0.2}Mn_2O_4$ σ (S/cm)**		**$Co_{0.67}Cu_{0.33}Mn_2O_4$ σ (S/cm)**	
	cooling	heating	cooling	heating	cooling	heating
600	0.9	0.9	4.6	4.6	9.4	9.3
700	3.3	3	11.1	10.4	22.0	21.5
750	7.1	6.7	18.8	17.4	42.3	42.2
800	13.3	13.1	29.3	27.9	49.4	48.6
850	18.6	18.5	35.4	35.3	55.3	54.9
Temperature(^{o}C)	**$Co_{0.5}Cu_{0.5}Mn_2O_4$ σ (S/cm)**		**$Co_{0.33}Cu_{0.67}Mn_2O_4$ σ (S/cm)**		**$CuMn_2O_4$ σ (S/cm)**	
	cooling	heating	cooling	heating	cooling	heating
600	12.9	12.7	20.0	20.0	34.7	34.7
700	35.8	35.7	49.6	47.5	80.1	82.1
750	58.0	58.0	81.4	78.3	92.8	92.8
800	64.2	64.3	90.7	90.8	104.0	103.6
850	70.3	70.6	100.5	101.0	116.7	115.7
Temperature(^{o}C)	**$Co_{1.5}Mn_{1.5}O_4$ σ (S/cm)**		**$Co_{1.2}Cu_{0.3}Mn_{1.5}O_4$ σ (S/cm)**		**$Co_{0.9}Cu_{0.6}Mn_{1.5}O_4$ σ (S/cm)**	
	cooling	heating	cooling	heating	cooling	heating
600	10.9	9.5	41	40.4	48.6	48.4
700	23.1	23.2	58.3	58.0	64.4	64.1
750	28.9	28.9	67.2	67	72.0	71.6
800	35.0	35.5	76.0	76.2	79.6	79.3
850	42.2	42.5	84.6	84.9	87.1	87.0
Temperature(^{o}C)	**$Co_{0.5}CuMn_{1.5}O_4$ σ (S/cm)**		**Co_2MnO_4 σ (S/cm)**		**$Co_{1.7}Cu_{0.3}MnO_4$ σ (S/cm)**	
	cooling	heating	cooling	heating	cooling	heating
600	38.0	38.0	19.4	17.7	30.6	31.1
700	53.9	52.9	39.4	38.3	51.5	52.1
750	62.6	62.3	53.2	52.5	64.1	65.3
800	71.6	71.7	70.1	68.9	77.8	78.2
850	80.6	81.2	87.9	86.6	91.8	91.7

Temperature(^{o}C)	**$Co_{1.37}Cu_{0.63}MnO_4$ σ (S/cm)**	
	cooling	heating
600	36.0	34.0
700	56.9	54.3
750	68.4	66.5
800	80.8	79.2
850	93.2	93.0

Appendix B XRD Results

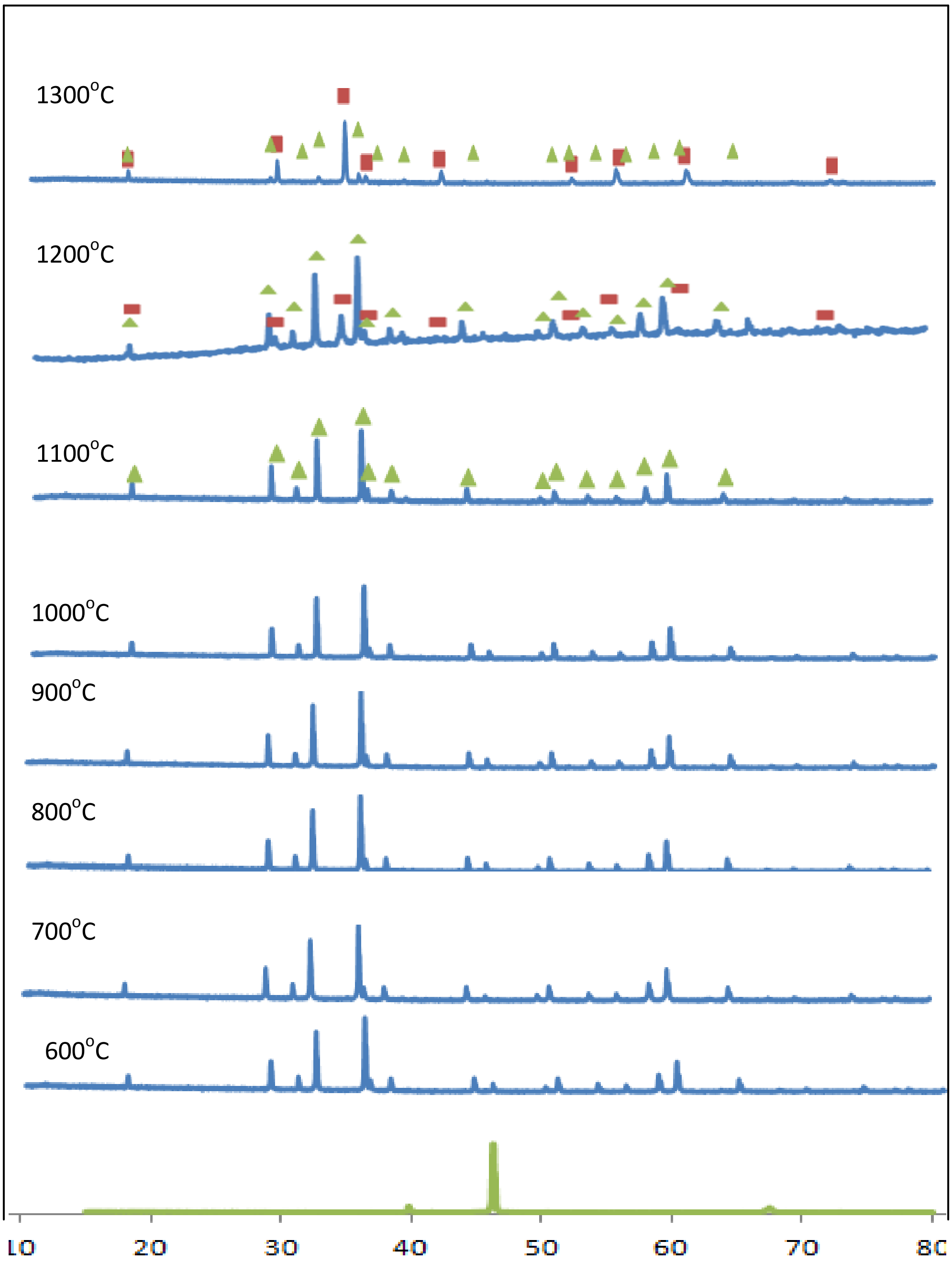

XRD results of $Zn_{0.4}Mn_{2.6}O_4$, 1300°C-1200°C, T+C; 1100°C-600°C, T.

🟥 cubic ▲ tetragonal

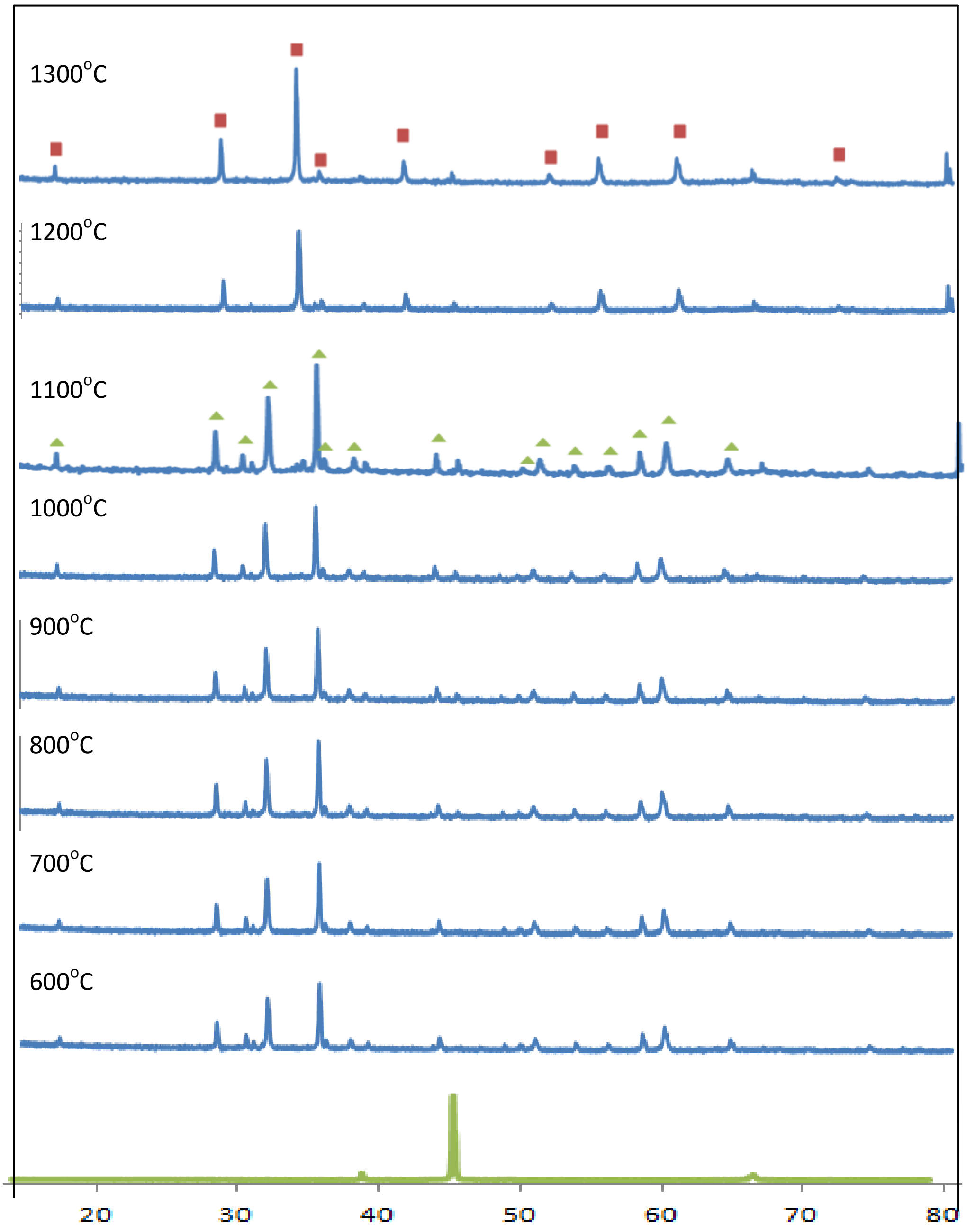

XRD results of $Zn_{0.6}Mn_{2.4}O_4$. 1300C, C; 1200C, C+T; 1100C-600C,T.

🟥 cubic ▲ tetragonal

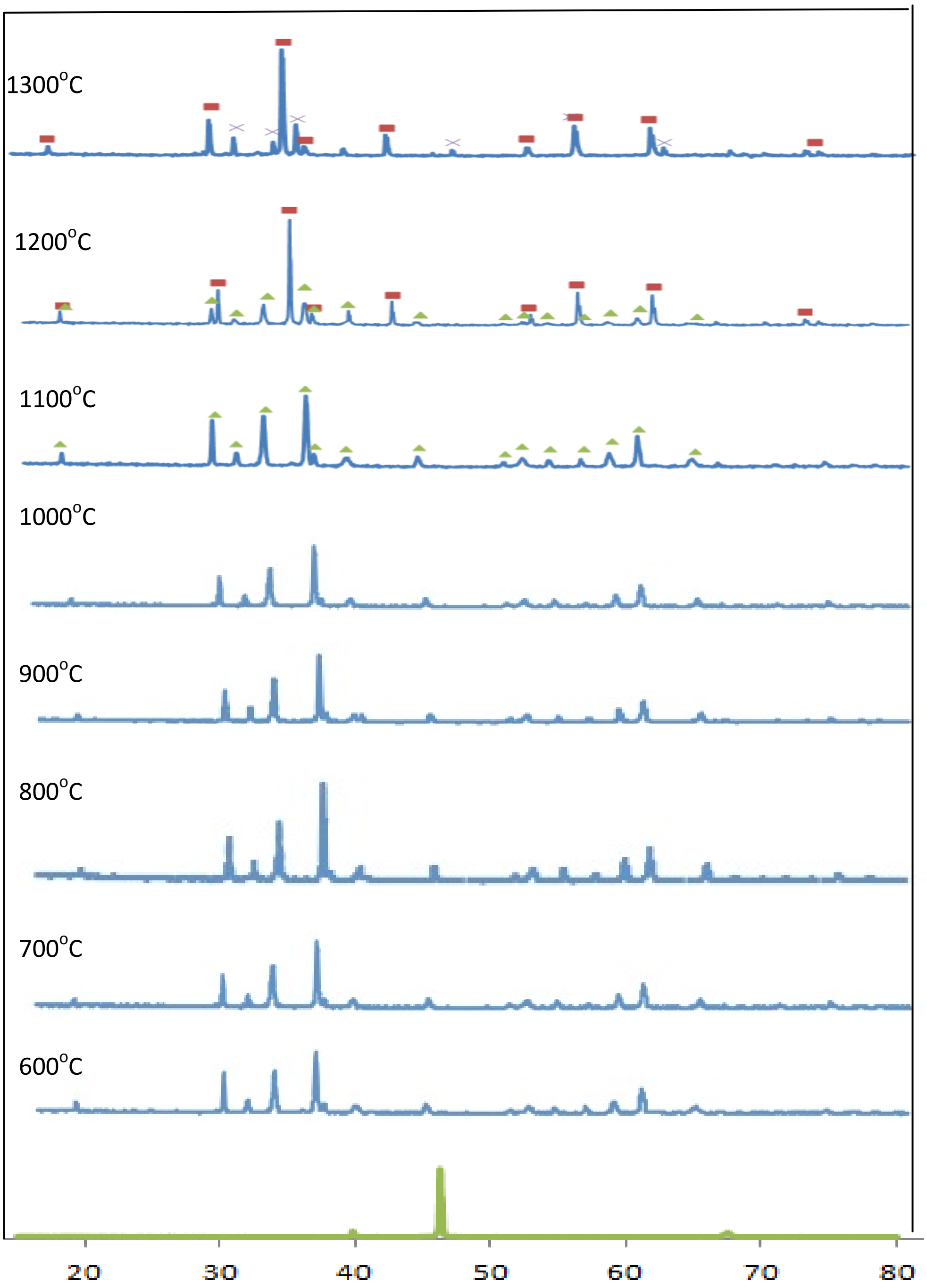

XRD results of $ZnMn_2O_4$. 1300°C, C + ZnO; 1200°C, C + T; 1100°C – 600°C, T.

🟥 cubic ▲ tetragonal × ZnO

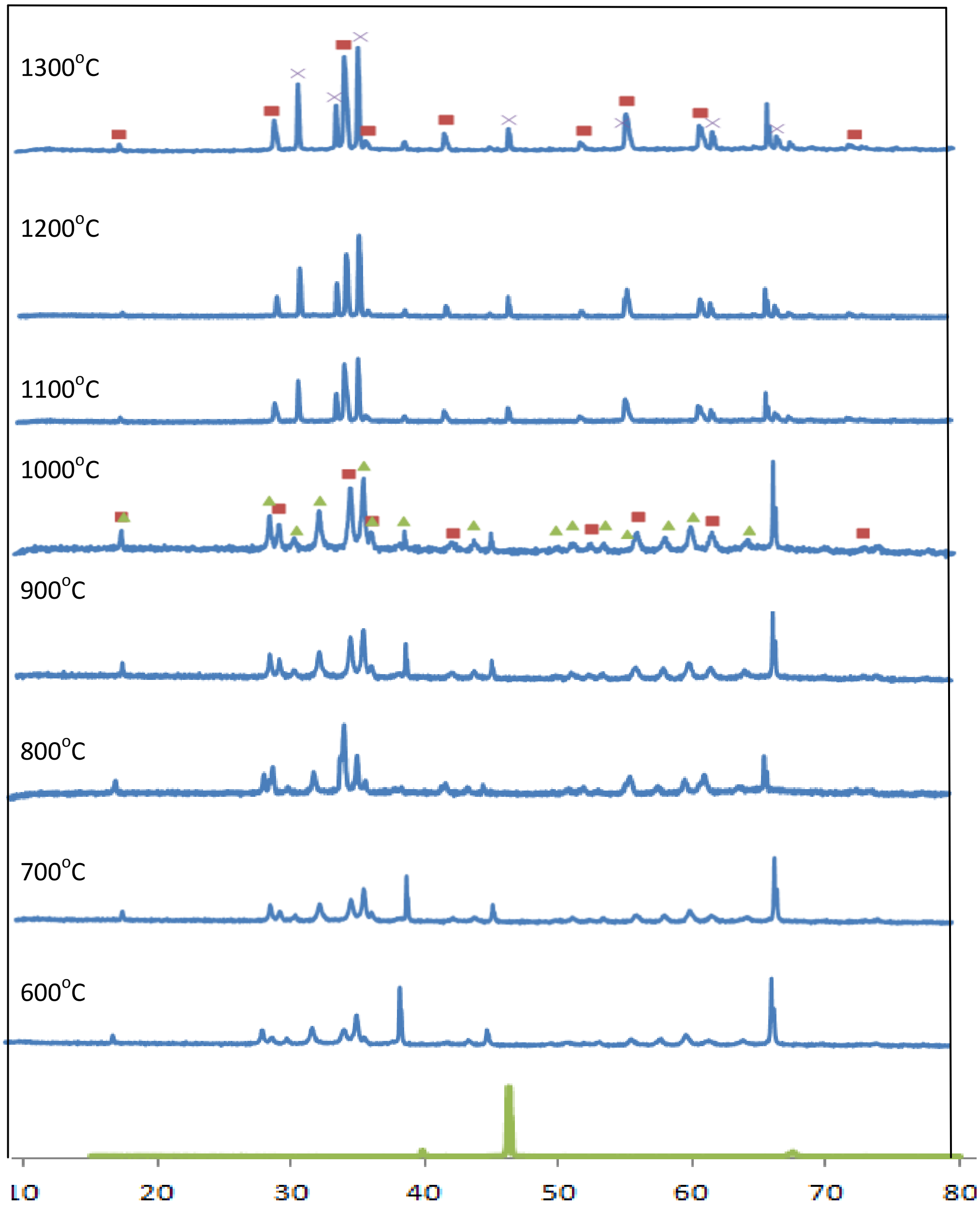

XRD results of $Zn_{1.2}Mn_{1.8}O_{4.}$ 1300 ^{O}- 1100^{O}C, C + ZnO; 1000^{O}C- 600^{O}C, T +C.

🟥 cubic ▲ tetragonal × ZnO

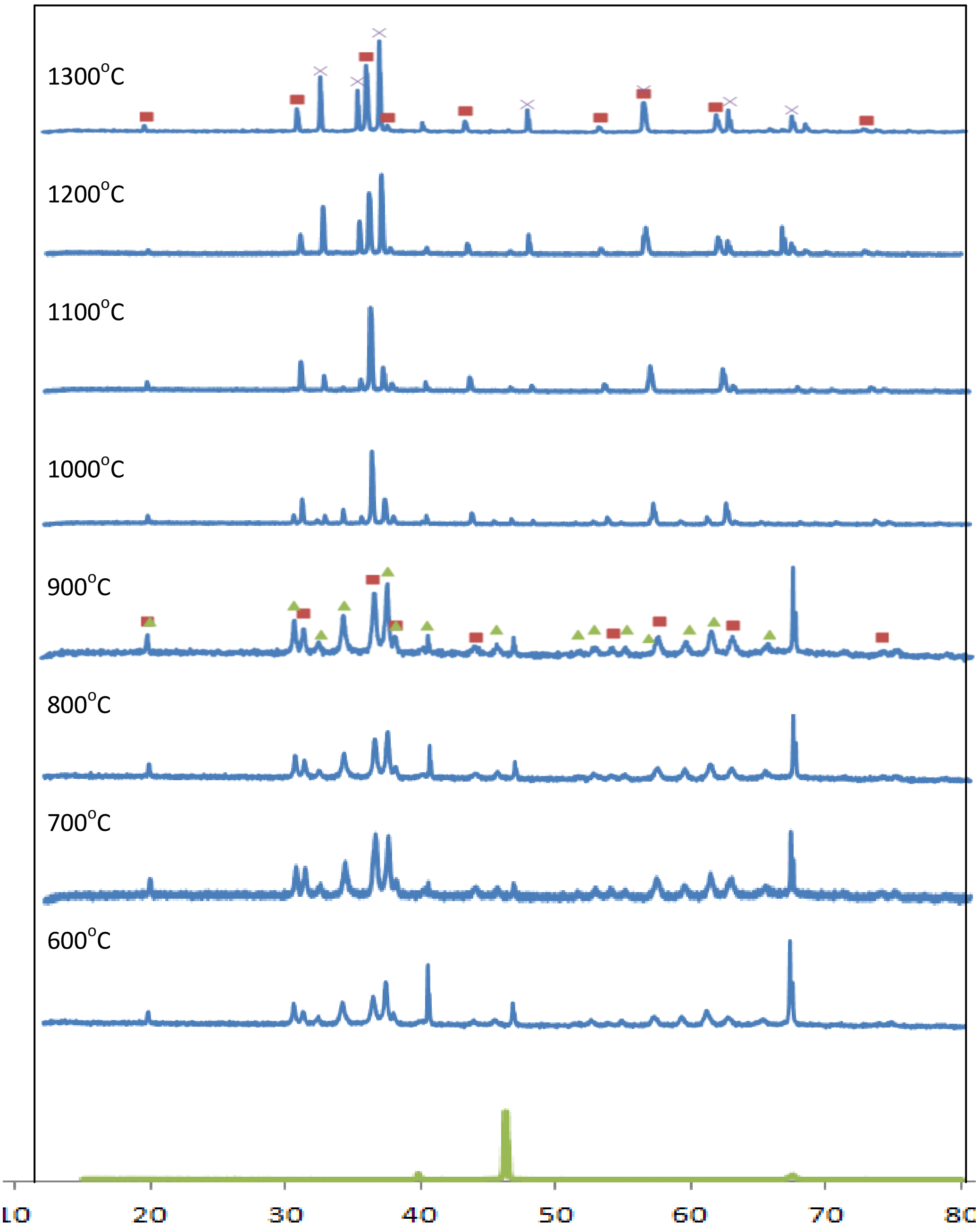

XRD results of $Zn_{1.4}Mn_{1.6}O_4$. 1300°C- 1100°C, C+ ZnO; 1000°C- 600°C, C+T

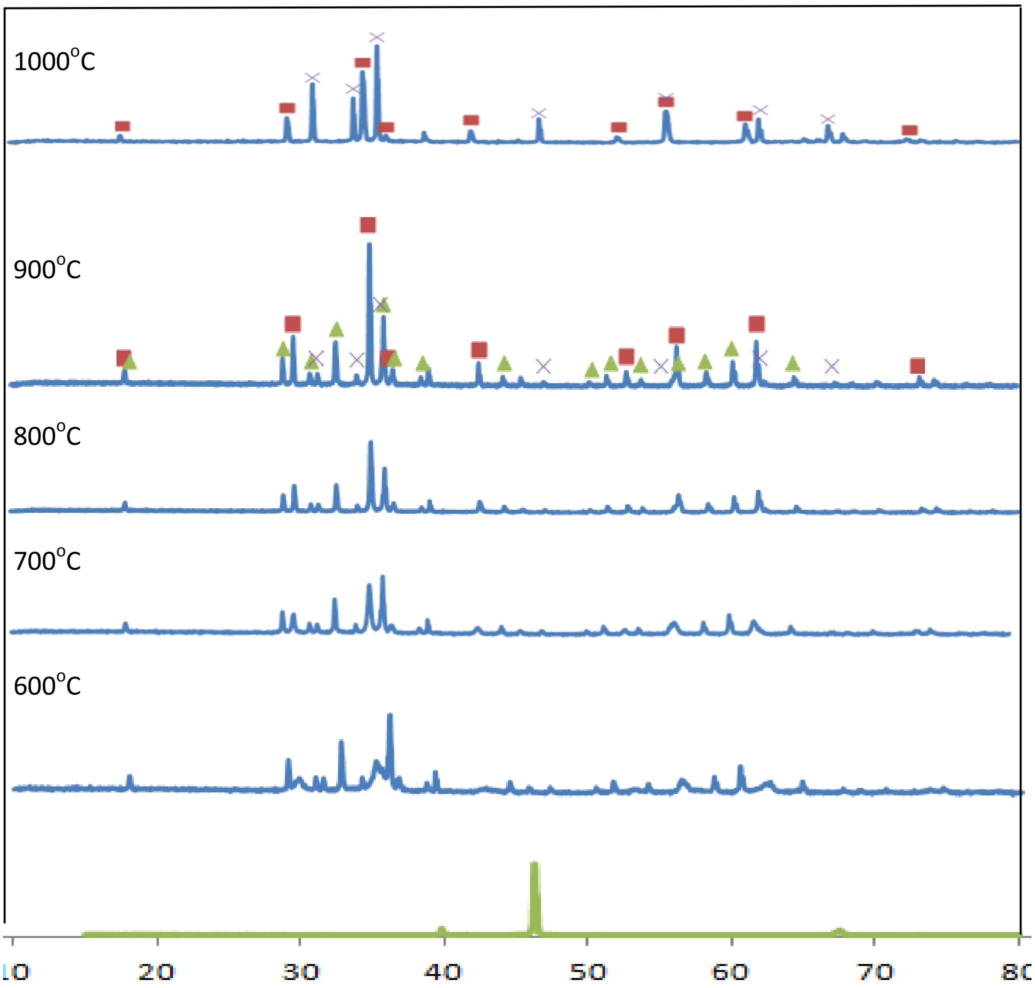

XRD results of $Zn_{1.5}Mn_{1.5}O_4$.1000°C, C+ ZnO; 900°C- 600°C, C+T+ZnO

🟥 cubic ▲ tetragonal × ZnO